RAS-PI3K Pathway in CAFs Shapes Physicochemical Properties of Tumor ECM to Impact Tumor Progression

Cristina Cuesta[1], Marta Alcón-Pérez[1], Jie Zheng[2], Nicole Procel[1], Rosa Ramírez-Cota[1], Dirk Fennema Galparsoro[3], Alejandro Rosell [1], Diana Loa-Meson[4], Belén Martínez-Castedo[1], Youssef Arafat[5], Héctor Sanz-Fraile[6], Vinothini Rajeeve[7], Diego Alonso-López[8], Robert E. Hynds[9,10], Charles Swanton[9,10], Jordi Alcaraz[6,11], Pedro Cutillas[7], Constantino C. Reyes-Aldasoro[5,12], Haiyun Wang[2], Esther Castellano[1*].

[1] Tumour-Stroma Signalling Lab, Centro de Investigación del Cáncer, Instituto de Biología Molecular y Celular del Cáncer, Consejo Superior de Investigaciones Científicas (CSIC)-Universidad de Salamanca, Campus Miguel de Unamuno, 37007 Salamanca, Spain.

[2] School of Life Sciences and Technology, Tongji University, Shanghai, China

[3] Advanced Cellular Analyses, Centro de Investigación del Cáncer, Instituto de Biología Molecular y Celular del Cáncer, Consejo Superior de Investigaciones Científicas (CSIC)-Universidad de Salamanca, Campus Miguel de Unamuno, 37007 Salamanca, Spain.

[4] Servicio de Experimentación Animal, Universidad de Salamanca, Campus Miguel de Unamuno, 37007 Salamanca, Spain.

[5] Department of Computer Science, City St George's, University of London, EC1V 0HB London, United Kingdom.

[6] Unit of Biophysics and Bioengineering, Department of Biomedicine, School of Medicine and Health Sciences, Universitat de Barcelona, Barcelona, Spain.

[7] Cell Signalling and Proteomics Laboratory, Centre for Cancer Evolution, Barts Cancer Institute, Queen Mary University of London, Charterhouse Square, London EC1M 6BQ, United Kingdom.

[8] Bioinformatics Unit, Centro de Investigación del Cáncer, Instituto de Biología Molecular y Celular del Cáncer, Consejo Superior de Investigaciones Científicas (CSIC)-Universidad de Salamanca, Campus Miguel de Unamuno, 37007 Salamanca, Spain.

[9] Cancer Research UK Lung Cancer Centre of Excellence, University College London Cancer Institute, London WC1E 6DD, United Kingdom

[10] Cancer Evolution and Genome Instability Laboratory, The Francis Crick Institute, London NW1 1AT, United Kingdom

[11] Institute for Bioengineering of Catalonia (IBEC), The Barcelona Institute for Science and Technology (BIST), Barcelona 08028, Spain.

[12] Integrated Pathology Unit, Division of Molecular Pathology, The Institute of Cancer Research, Sutton, United Kingdom

[*] Correspondence: ecastellano@usal.es

Key words: RAS, p110α, phosphatidylinositol 3-kinase, PI3K, cancer associated fibroblasts, myoCAFs, extracellular matrix (ECM), tumor microenvironment.

ABSTRACT

Cancer-associated fibroblasts (CAFs) are key regulators of the tumor microenvironment, promoting tumor progression through extracellular matrix (ECM) remodeling and paracrine signaling, but the signaling pathways controlling CAF function remain incompletely defined. Here, we demonstrate that RAS-PI3K signaling plays a central role in CAF activation and ECM remodeling by promoting collagen crosslinking, fibronectin organization, and glycoprotein deposition at least partially through the activation of YAP. Disruption of RAS-PI3K interaction in CAFs leads to structurally and mechanically defective ECMs that impair tumor cell adhesion, migration, and proliferation. *In vivo*, fibroblast-specific deletion of RAS-PI3K reduces tumor burden in different models of KRAS-driven lung cancer, limits ECM deposition, and enhances the response to chemotherapy and RAS-targeted therapies in lung adenocarcinoma models. These findings position RAS-PI3K signaling as a critical regulator of CAF function and ECM remodeling, highlighting a drug repurposing therapeutic strategy to disrupt tumor-stroma interactions and improve treatment outcomes.

INTRODUCTION

Cancer progression is a complex process in which the interaction between tumor cells and their surrounding microenvironment, known as the tumor stroma, plays a pivotal role. Among the key stromal components are cancer-associated fibroblasts (CAFs) [1, 2]. Recent advances in the field show that these activated fibroblasts can no longer be considered passive bystanders, but rather active collaborators that fuel tumor growth, invasion, and metastasis through diverse mechanisms [1, 3-5].

CAFs represent a heterogeneous population with distinct origins and functional specializations that contribute to tumor progression. Among the major subtypes identified [6, 7], inflammatory CAFs (iCAFs) are characterized by the secretion of cytokines and growth factors that modulate immune responses and paracrine signaling, while antigen-presenting CAFs (apCAFs) can influence immune surveillance through MHC-II-mediated antigen presentation. Myofibroblastic CAFs (myoCAFs), on the other hand, specialize in ECM remodeling and mechanical regulation. MyoCAFs are characterized by the expression of contractile proteins such as α-smooth muscle actin (α-SMA), which enable them to generate mechanical tension. One of their most critical functions is the remodeling of the extracellular matrix (ECM), a dynamic network of structural proteins and polysaccharides that provides both mechanical support and biochemical signals to cells [8-10]. myoCAFs modify ECM stiffness, composition, and organization, transforming it from a physical barrier into a permissive niche that facilitates tumor progression [9, 11]. These changes not only promote tumor cell proliferation, survival, and migration but also influence angiogenesis and suppress anti-tumor immune responses, further enhancing tumor progression[12, 13].

By disrupting ECM remodeling, it may be possible to impair tumor growth and invasion while also enhancing the efficacy of existing treatments. [1, 14, 15]. However, the signaling pathways that regulate myoCAF activation and ECM remodeling remain poorly understood, limiting the development of effective stromal-targeting therapies. Early attempts to therapeutically modulate the stroma, including strategies to deplete fibroblasts or block Hedgehog signaling, yielded mixed or detrimental results in clinical trials due to unanticipated effects on ECM homeostasis and immune suppression[16-19]. These

setbacks underscore the importance of elucidating the molecular mechanisms governing CAF plasticity and ECM regulation to design therapies that normalize rather than eliminate stromal components, preserving tumor-restraining functions while suppressing tumor-promoting activity.

RAS proteins are central drivers of cancer progression, primarily through their well-characterized effects in tumor cells. More recently, attention has been played to the role of mutant RAS in shaping the tumor microenvironment[20, 21]. Existing evidence proves that RAS signaling regulates immune cells' recruitment, activation, and differentiation while assisting immune surveillance evasion by tumor cells [22-25]. Studies using pancreatic cancer models have shown that KRAS mediates the activation of fibroblasts through Hedgehog signaling[26-28], and the impact of KRAS on the regulation of the most potent angiogenesis inducer VEGF has been extensively studied in different models[29-31]. A direct role of mutant KRAS on the modulation of extracellular matrix (ECM) properties has also been described in lung and pancreatic cancer models, where it promotes gene expression programs that result in ECM remodeling and collagen degradation by MMPs, thereby enabling invasive tumor growth through elimination of physical restraints [32-34].

While much of this work has focused on oncogenic RAS, the role of wild-type (WT) RAS signaling within stromal cells remains less explored. Emerging evidence suggests that WT RAS signaling may also contribute to tumor progression through its downstream effectors, including PI3K, which regulates cytoskeletal organization, adhesion, and contractility in fibroblasts. In lung cancer, disruption of RAS-PI3K signaling in the stroma significantly reduces tumor burden, highlighting its potential role in modulating the tumor microenvironment[35, 36].

Given the central role of PI3K in fibroblast biology and its regulation of cytoskeletal dynamics and ECM remodeling, we hypothesized that RAS-PI3K signaling in CAFs sustains tumor-promoting functions by controlling ECM structure and composition and investigated how disrupting the interaction between RAS and PI3K specifically in fibroblasts affects CAF activation, ECM remodeling, and tumor progression. We further examined whether these ECM alterations enhance responses to chemotherapy and targeted therapies to evaluate the therapeutic potential of targeting stromal signaling.

RESULTS

RAS-PI3K Signaling Regulates CAF Activation Through YAP-Dependent Transcriptional Programs and Actin Cytoskeletal Organization

Previous studies have shown that disrupting the interaction between RAS and PI3K not only prevents lung tumor initiation but also significantly slows the progression of established tumors [35, 37]. While these effects have been partly attributed to intrinsic alterations in tumor cells, evidence also points to a significant contribution from the tumor microenvironment[35, 36], suggesting that the stromal compartment may play a key role in sustaining tumor growth. Among stromal cells, cancer-associated fibroblasts (CAFs) are critical regulators of tumor progression through ECM remodeling, immune modulation, and paracrine signaling. Given that RAS-PI3K signaling is an important regulator of fibroblast biology[37, 38], we hypothesized that the disruption of this signaling axis in CAFs could contribute to the impaired tumor growth observed after RAS-PI3K disruption. Specifically, we aimed to determine whether RAS-PI3K signaling in CAFs is required to support ECM remodeling and other pro-tumorigenic functions that promote tumor progression. Understanding this dependency could reveal novel therapeutic vulnerabilities within the tumor microenvironment.

To investigate whether the previously observed effects of RAS-PI3K disruption on tumor growth could be mediated, at least in part, by alterations in the stromal compartment, we used the RBD mouse model, in which the interaction between p110α and RAS (*Pik3ca*^{RBD}) is disrupted through two-point mutations (T208D and K227A) in the endogenous *Pik3ca* gene[37]. Wild-type (*Pik3ca*^{WT}) and *Pik3ca*^{RBD} mice were bred with mice carrying floxed *Pik3ca* alleles and Cre-ERT2 recombinase alleles targeted to the Rosa26 locus (*Pik3ca*$^{RBD/flox}$) and further crossed with Kras^{LA2} mice[39], which spontaneously develop lung adenomas. This breeding strategy allowed us to generate inducible knockouts in which flox removal is achieved with tamoxifen treatment (*Pik3ca*$^{RBD/-}$).

After 16 weeks of tamoxifen treatment, lungs were harvested and analyzed for CAF activation markers. α-SMA immunostaining revealed a marked reduction in α-SMA-positive cells in the lungs of *Pik3ca*$^{RBD/-}$

mice compared to their *Pik3ca*$^{WT/-}$ counterparts (Fig. 1A). Similarly, Sirius Red staining showed a significant decrease in collagen deposition in the *Pik3ca*$^{RBD/-}$ group (Fig. 1A).

Next, we explored whether the impaired CAF activation observed in *Pik3ca*$^{RBD/-}$ tumors could be due to alterations in TGF-β signaling, the main cytokine linked to activation of fibroblasts toward CAFs[40]. We analyzed both canonical and non-canonical TGF-β signaling pathways in fibrobla

sts lacking RAS-PI3K interaction isolated and immortalized from the *Pik3ca*^{RBD} model[37] (referred to as RBD from now on). Western blot analysis of Smad2/3 phosphorylation revealed no significant differences between RBD and control cells (Supplementary Fig. S1A). In contrast, RBD cells showed a marked reduction in non-canonical TGF-β signaling markers pAKT and pRPS6 levels compared to controls, while pERK levels remained unchanged (Fig. 1B). Additionally, no differences were observed in cell surface levels of TGF-β receptor (TGFBR2) (Supplementary Fig. S1B).

To gain deeper insight into the molecular mechanisms underlying these defects, we performed a phosphoproteomic analysis on tumors from *Pik3ca*$^{RBD/-}$ and *Pik3ca*$^{WT/-}$ mice, as well as tumors from wild-type mice treated with the p110α-specific inhibitor alpelisib to compare the impact of genetic disruption and pharmacological inhibition of RAS-PI3K signaling. We identified 266 differentially phosphorylated peptides in *Pik3ca*$^{RBD/-}$ tumors compared to controls, with 208 upregulated and 58 downregulated by at least 2-fold change (Fig. 1C and supplementary Table S1, see methods). Similarly, alpelisib-treated tumors, displayed 241 altered phosphorylated proteins (Supplementary Fig. S1C) with 163 (67.6%) proteins presenting similar changes in the two experimental settings (Supplementary Fig. S1D and supplementary Table S2), suggesting that pharmacological inhibition of p110α has the potential to recapitulate the molecular alterations observed with genetic disruption.

Among the proteins showing decreased phosphorylation in both experiments were YAP, vimentin, paxillin (PXN), and filamin A (FLNA) (Supplementary Table S1), all of which are involved in cytoskeletal organization and structural dynamics. Conversely, proteins with increases in phosphorylation included LIMCH1, MYH9, and TJP2, further pointing to disruptions in cytoskeletal proteins and cell-cell adhesion

mechanisms. Ontology enrichment analysis highlighted changes in pathways governing actin filament organization, cellular polarity, and cytoskeletal stabilization (Fig. 1D and supplementary Fig. 1E).

The actin cytoskeleton plays a pivotal role in properties essential for CAF activation and function[41-43]. The reduced levels of α-SMA, vimentin, and YAP in *Pik3ca*$^{RBD/-}$ tumors, gave weight to the hypothesis that RAS-PI3K disruption compromises CAF functionality. To test this, we examined expression of these proteins in RBD fibroblasts stimulated with TGF-β or conditioned medium from the KRAS-mutant lung cancer cell KPB6. Upon stimulation with either TGF-β or conditioned medium, RBD fibroblasts displayed a significant reduction in the expression of α-SMA, vimentin, and YAP compared with WT controls (Supplementary Fig. S1F). Similar results were obtained by immunofluorescence (IF) analysis (Fig. 1E and 1F and Supplementary S1G). Importantly, reintroducing functional p110α into RBD cells fully rescued the expression of these markers, restoring expression levels to those of WT cells. Consistently, pharmacological inhibition of p110α with alpelisib in WT fibroblasts replicated the phenotype observed in RBD cells, leading to a marked reduction in all the three markers, thus highlighting the dependence of CAF activation on an intact RAS-PI3K signaling.

We next evaluated whether the observed decrease in YAP expression and phosphorylation functionally leads to a decrease in its transcriptional activity, which is tightly linked to actin cytoskeletal dynamics [42, 44-46]. Luciferase reporter assays demonstrated a significant reduction in YAP activity in RBD fibroblasts following TGF-β stimulation or exposure to conditioned medium from KPB6 cells (Fig. 1G). Consistently, expression of YAP target genes *Ctgf* and *Tagln2* was significantly downregulated, while, surprisingly, the expression of *Cyr61* and *Ankrd1* remained unaffected (Supplementary Fig. S1H), suggesting that that RAS-PI3K disruption selectively impairs specific YAP-dependent transcriptional programs rather than inducing a global suppression of YAP activity.

The phosphoproteomic data suggested an impairment in actin cytoskeleton as a consequence to RAS-PI3K disruption. To determine if this dysregulation has phenotypic consequences in terms of CAF deficient activation, we next investigated whether RBD CAFs could adopted the elongated, spindle-shaped morphology, typical from CAFs in response to TGF-β activation. WT fibroblasts displayed the

expected spindle-like morphology. In contrast, RBD fibroblasts exhibited a more rounded shape (Fig. 1H). Notably, impairment of Yap translocation to the nucleus with verteporfin (Supplementary Fig. S1G), resulted in a similarly rounded morphology (Fig. 1H).

Actin fractionation assays further revealed a significant reduction in filamentous actin (F-actin) levels in RBD fibroblasts compared to WT controls (Fig. 1I, Supplementary Fig. S1I), whereas globular actin (G-actin) levels remained unchanged (Supplementary Fig. S1J). Notably, treatment of WT fibroblasts with verteporfin recapitulated this phenotype, mirroring the reduction in F-actin observed in RBD cells. To further confirm that RAS-PI3K, through YAP regulation of actin cytoskeleton, impairs CAF activation, we next analyzed the expression of genes associated with CAF activation and function. Fibroblasts were stimulated with TGF-β or conditioned medium from KPB6 cells and the expression of *Ctgf* and *Tagln* was included as controls to validate the impact of RAS-PI3K and verteporfin on YAP-regulated genes (Supplementary Fig. S1H). Beyond these controls, expression of genes involved in ECM remodeling and CAF activation, including *Postn*, *Tgfb1*, *Tnc*, *Mmp2*, *Mmp3*, and *Mmp10*, was significantly lower in RBD fibroblasts compared with WT (Fig. 1J and Supplementary Fig. S1K). Interestingly, expression of *Fap*, *Fsp1*, and *Snail* was upregulated in RBD fibroblasts, suggesting potential compensatory mechanisms or a shift toward an alternative fibroblast phenotype. Treatment of WT fibroblasts with verteporfin resulted in a general decrease in the expression CAF activation genes, with several markers, such as *Ctgf* and *Tagln*, expressed at levels comparable to those observed in RBD cells (Fig. 1J and Supplementary Fig. S1K). However, genes expressed at higher levels in the RBD fibroblasts (*Fap*, *Fsp1*, and *Snail*) were downregulated upon YAP inhibition (Fig. 1J and Supplementary Fig. S1K), indicating that their regulation may be independent of RAS-PI3K-YAP regulation.

RAS-PI3K Signaling Loss Impairs TGF-β Pathways and ECM-Related Transcriptional Programs in CAFs

The results above strongly suggest that RAS-PI3K signaling is a central regulator of CAF activation, with broader implications for stromal-tumor crosstalk within the tumor microenvironment. To identify downstream transcriptional programs relevant for CAF function and influenced by this pathway, we

performed RNA sequencing (RNA-seq) on RBD and control fibroblasts, both under basal conditions and following TGF-β stimulation, to capture gene expression changes associated with RAS-PI3K disruption. RNA-seq analysis revealed substantial transcriptional reprogramming in RBD cells compared to controls. Using an FDR cutoff of 0.02 and a fold change (FC) threshold of 1.5, we identified 1151 differentially expressed genes (DEGs) in untreated RBD fibroblasts (Supplementary Table S3), with 677 upregulated and 474 downregulated (Figure 2A and Supplementary Fig. S2A). Upon TGF-β stimulation, 922 DEGs were identified (Supplementary Table S4), with 440 upregulated and 482 downregulated (Figure 2A and Supplementary Fig. S2A).

Interestingly, 661 DEGs overlapped between untreated and TGF-β-treated conditions, suggesting a core transcriptional signature associated with RAS-PI3K disruption (Fig. 2B). Among these overlapping genes, 330 were consistently upregulated and 331 (Supplementary Fig. S2B), reinforcing the persistence of RAS-PI3K-dependent programs, regardless of TGF-β stimulation.

Functional enrichment analysis of DEGs revealed distinct transcriptional programs in untreated and TGF-β-stimulated conditions, with a shared emphasis on ECM remodeling, tissue organization, and cell adhesion. In untreated RBD cells, upregulated genes were enriched in pathways related to receptor complexes, lipid localization, and endopeptidase activity, reflecting intrinsic disruptions in signaling and cell communication (Supplementary Fig. S2C). Conversely, downregulated genes were enriched in ECM-related terms, such as extracellular matrix structural constituents, integrin binding, and contractile fiber organization, highlighting defects in ECM assembly and adhesion mechanisms (Supplementary Fig. S2C).

Upon TGF-β stimulation, transcriptional profiles shifted toward pathways associated with tumor-associated ECM remodeling and tissue dynamics. Upregulated genes included ECM-specific terms, such as collagen-containing ECM and tissue remodeling, as well as developmental pathways and signaling processes (Fig. 2C). Downregulated genes were also enriched for ECM organization, adhesion molecules, and basement membrane components, reflecting broader impairments in matrix remodeling (Fig. 2C).

Further supporting these findings, GSEA analysis revealed significant enrichment of key ECM-related pathways in WT fibroblasts. Specifically, Collagen Degradation (Fig. 2D) and Degradation of ECM (Fig. 2E) were enriched under both untreated and TGF-β-stimulated conditions, indicating a consistent defect in ECM turnover and maintenance in RBD fibroblasts. The Crosslinking of Collagen Fibrils pathway (Fig. 2F), essential for structural ECM integrity, was also enriched in WT cells across both conditions, highlighting an impaired ability to stabilize collagen fibers. Additionally, the Matrix Metalloproteinases pathway (Fig. 2G) was prominently enriched in WT fibroblasts following TGF-β stimulation, reflecting the failure of RBD cells to engage dynamic ECM remodeling processes critical for tumor progression.

The absence of these enriched pathways in RBD fibroblasts suggests a deficiency in genes associated with ECM remodeling, resulting in significant alterations in ECM properties. These include reduced collagen degradation, impaired fiber crosslinking, and disorganized matrix architecture. Such deficiencies align with experimental observations of shorter, less aligned collagen fibers and lower matrix stiffness in RBD-derived matrices, emphasizing the central role of RAS-PI3K signaling in maintaining ECM structure and function.

The overlap of ECM-related pathways between untreated and TGF-β-stimulated conditions underscores that RAS-PI3K signaling is essential for sustaining ECM programs both at baseline and in response to pro-tumorigenic cues. While intrinsic transcriptional changes in RBD cells highlight baseline defects in ECM integrity, TGF-β-induced programs further reveal their inability to activate dynamic ECM remodeling processes required for tumor progression. Together, these findings demonstrate that RAS-PI3K signaling orchestrates the structural and functional integrity of the ECM, positioning it as a critical regulator of CAF-mediated modulation of the tumor microenvironment.

Disruption of RAS-PI3K Impairs CAF-Mediated ECM Production and Remodeling

Since RNAseq data suggested that ECM remodeling is a key function controlled by RAS-PI3K signaling in CAFs, we next evaluated whether RAS-PI3K disruption specifically alters collagen production, remodeling, and structural organization.

To this end, we assessed collagen gel contraction. Control and RBD fibroblasts were embedded in collagen gels and activated with TGF-β. Analysis of the contraction index revealed that WT fibroblasts efficiently contracted collagen gels, whereas RBD fibroblasts exhibited a marked inability to do so (Fig. 3A). This defect was fully rescued by reintroducing functional p110α into RBD cells, restoring collagen contraction to WT levels. Conversely, WT fibroblasts treated with the p110α-specific inhibitor alpelisib lost the ability to contract collagen gels, recapitulating the defects observed in RBD cells (Fig. 3A).

Next, we analyzed the expression of *Lox* and *Plod*, two enzymes critical for collagen crosslinking and maturation. Both genes were significantly downregulated in RBD fibroblasts compared to WT controls, with stronger effects under conditioned medium stimulation from KRAS-mutant KPB6 cells than in TGF-β activated CAFs, suggesting that RAS-PI3K disruption may impair collagen crosslinking more severely in the context of tumor-derived signals (Fig. 3B). To determine whether this effect could be mediated through YAP-dependent mechanisms, we treated WT fibroblasts with verteporfin. Similar to RBD cells, verteporfin-treated WT fibroblasts exhibited a significant reduction in *Lox* and *Plod* expression relative to controls. While the reduction in response to TGF-β was comparable between RBD and verteporfin-treated cells, the effect was slightly more pronounced under conditioned medium stimulation in the verteporfin group, although this difference did not reach statistical significance (Fig. 3B).

We next sought to study whether the defects observed in collagen remodeling extended to the *de novo* production of collagen. For this, we utilized a glutaraldehyde crosslinked gelatin-based culture system, which allows for the assessment of newly synthesized ECM components[47], or 'CAF-derived matrices' (CDMs). WT and RBD fibroblasts activated with TGF-β were cultured to produce and remodel ECM, and Sirius Red staining was analyzed to evaluate collagen content and fiber organization.

Collagen fibers in CDMs generated by RBD fibroblasts were significantly shorter and thinner than those produced by WT controls (Fig. 3C and 3D). Reintroducing functional p110α expression into RBD fibroblasts rescued fiber length, restoring it to WT levels, but failed to fully recover fiber thickness. Conversely, treatment of WT fibroblasts with alpelisib resulted in matrices enriched in short fibers,

although fiber thickness was not changed (Fig. 3C and 3D), highlighting the selective role of RAS-PI3K signaling in regulating distinct aspects of collagen matrix formation.

Finally, we attempted to validate these findings *in vivo*, implanting collagen plugs embedded with WT or RBD TGF-β-activated fibroblasts into the flanks of C57BL/6 mice. Sirius Red staining of retrieved plugs showed that WT CAFs produced long, straight collagen fibers. In contrast, RBD CAFs generated short, curly collagen fibers (Fig. 3E), further supporting the role of RAS-PI3K signaling for the structural organization of collagen fibers.

Building on these data, we also investigated whether RAS-PI3K disruption similarly affects the deposition and organization of fibronectin, another key ECM-structural component. Using the same glutaraldehyde crosslinked gelatin culture system, quantitative data showed that RBD fibroblasts produced significantly thinner matrices with less aligned fibronectin fibers compared to their WT counterparts (Fig. 3F and 3G). Reintroduction of functional p110α in RBD fibroblasts restored fiber alignment to WT levels but did not rescue matrix thickness. Conversely, treatment of WT fibroblasts with alpelisib resulted in thinner and disorganized matrices, closely mimicking the phenotype observed in RBD fibroblasts (Fig. 3F and 3G). We also observed that these defects persisted in a tumor-relevant context. Using co-cultures of WT or RBD CAFs together with the KRAS-mutant lung cancer cell lines KPB6 and LKR13 we observed that matrices generated in co-culture with RBD fibroblasts were less fibrous, exhibited reduced fibronectin content, and showed signs of disorganization compared to those formed with WT fibroblasts (Supplementary Fig. S3B).

Considering these differences, we next evaluated mechanical properties of these CDMs, as well as accessibility and binding capacity. Mechanical analysis of these CDMs revealed that matrices produced by RBD fibroblasts were significantly softer compared to those generated by WT fibroblasts (Fig. 3H). Reintroduction of functional p110α fully restored matrix stiffness to WT levels, while treatment of WT fibroblasts with alpelisib led to softer matrices (Fig. 3H).

To assess the accessibility and binding capacity of ECM fibers, we performed FLIM analysis using the molecular rotor DCVJ (9-(2,2-Dicyanovinyl)julolidine). This fluorescent dye exhibits viscosity-

dependent fluorescence quantum yield, making it a sensitive probe for environmental changes. In low-viscosity environments, DCVJ dissipates absorbed energy non-radiatively by rotating the bond between its two aromatic rings. However, in high-viscosity environments or when sterically hindered upon binding, its fluorescence lifetime and quantum yield increase[48, 49]. WT and RBD CDMs were stained with DCVJ at different concentrations (200, 300, 500 and 1000 nM), and fluorescence lifetime micrographs were obtained. Protein fibers and cellular debris exhibited distinct fluorescence lifetimes, with debris consistently displaying the longest lifetimes across all conditions. At lower concentrations, WT and RBD fibers showed similar fluorescence lifetimes; however, as dye concentration increased, RBD fibers exhibited significantly shorter fluorescence lifetimes, highlighted by blue-colored regions (Fig. 3I). To quantify these differences, we analyzed DCVJ behavior in glycerol (Supplementary Fig. S3C) and constructed phasor plots for all concentrations and both samples. The alignment of phasors along a straight line within the universal circle suggested that DCVJ exhibited a double-exponential fluorescence decay, with two distinct lifetimes ($\tau1$ = 1.9 ns and $\tau2$ = 0.3 ns). These behaviors are characteristic of molecular rotors, where fluorescence lifetimes depend on rotational freedom. Comparisons with DCVJ behavior in glycerol (Supplementary Figure S3C) indicated that $\tau2$ (0.3 ns) corresponded to unbound molecules, while $\tau1$ (1.9 ns) represented dye molecules bound to ECM fibers, where steric hindrance restricted rotational freedom[50].

Using a linear addition model based on phasor distribution[51], we calculated the fraction of dye molecules bound to ECM fibers at each concentration. Lineweaver-Burk analysis (inset) provided estimates of the binding constant and the relative number of binding sites for WT and RBD fibers (Fig. 3I, inset graph). When evaluating the binding rate (Vmax) of the rotor to the fibers (Y-axis intercept), we found that WT fibers exhibited a V_{max} was 1.0 x 10^{-6} M, whereas RBD fibers displayed a lower V_{max} of 0.3 x 10^{-6} M. We next calculated the binding affinity (K_d) of the rotor to the fibers (X-axis intercept), obtaining values of 2.9 x 10^{-6} s^{-1} for WT and 1.08 x 10^{-6} s^{-1} for RBD fibers. Both parameters were approximately three times higher in WT fibers compared to RBD fibers, indicating that WT-derived ECM fibers exhibit greater structural organization, providing more binding sites and higher

permeability for molecular probes. In contrast, the reduced binding observed in RBD-derived matrices reflects structural defects, including lower density and altered organization, consistent with previously observed reductions in collagen fiber length, thickness, and alignment.

Finally, we wondered if CDMs formed by human CAFs isolated from human lung adenocarcinomas (hCAFs) treated with alpelisib also displayed alteration in their ability to remodel and form matrices. Data showed that inhibition of p110α impaired ability to contract gels (Fig. 3J) and led to the production of thinner matrices with disorganized and less aligned fibronectin fibers (Fig. 3K and 3L), underscoring a conserved role for RAS-PI3K signaling in ECM regulation across species.

CDMs produced by PI3K^{RBD} CAFs are defective in glycoproteins

We next aimed to further investigate investigate the changes in ECM composition induced by disruption of RAS-PI3K in CAFs. CDMs produced by RBD and WT CAFs were subjected to a matrisome analysis[52] to determine protein composition. Principal component analysis (PCA) of the expression profiles grouped samples according to their description, showing good inter-sample reproducibility (Supplementary Fig. 4A). Using a Student's t-test ($\log_2$ fold change > 0.5, p value < 0.05), we identified 515 differentially expressed proteins (432 up-regulated and 83 down-regulated). Filtering these proteins through MatrisomeDB[53] and excluding non-core or non-associated ECM proteins yielded 35 differentially expressed ECM components (24 up-regulated and 11 down-regulated) (Fig. 4A-B and Supplementary Table S5). Among these, 20 were classified as core matrisome components and 15 as matrisome-related components.

Further classification of the 35 matrisome components revealed that ≈40% of the identified components belonged to the ECM glycoproteins category (Fig. 4C). Interestingly, collagens and ECM-affiliated proteins were exclusively up-regulated in RBD derived ECMs, while secreted factors were predominantly down-regulated. Glycoproteins were represented in both up-regulated and down-regulated groups, but were more frequently down-regulated (Supplementary Fig. S4B). Pathway enrichment analysis highlighted significant enrichment of collagen matrix-related and ECM structural pathways among the up-regulated components (Fig. 4D). Conversely, down-regulated components

were enriched in pathways related to cell-matrix adhesion, TGF-β response, and binding interactions (Fig. 4D). These compositional changes further reinforce the structural and mechanical alterations observed in collagen and fibronectin matrices, including reductions in fiber alignment, thickness, and matrix stiffness. These findings underscore the role of RAS-PI3K signaling in maintaining ECM organization and mechanical properties that are critical for tumor progression and CAF functionality.

Defects in CDM specific glycoprotein content in RBD CDMs were validated by Alcian Blue stainig, a specific method for detecting ECM glycosylation (Fig. 4E). Reintroduction of functional p110α in RBD fibroblasts partially rescued GAG deposition, while Alpelisib treatment in WT fibroblasts mimicked the RBD phenotype.

We selected 10 glycoproteins for further expression validation, based on their differential expression in the matrisome analysis: *Igsf10*, *Tnn*, *Lamc1*, *Ltbp3*, *Efemp2*, *Aebp1*, *Mfap5*, *Fbn1*, *Mgp*, and *Matn2*. Consistent with the proteomic data, qPCR analysis revealed a significant downregulation of *Igsf10* and *Tnn* in RBD fibroblasts under both TGF-β stimulation and KPB6-conditioned medium, confirming their decreased expression at the transcriptional level (Fig. 4F). Additionally, *Mfap5* was significantly downregulated specifically in response to KPB6-conditioned medium, suggesting that tumor-derived factors may exacerbate these effects (Fig. 4F). Conversely, genes upregulated in the matrisome analysis, including *Aebp1* and *Mgp*, also showed significant transcriptional upregulation in RBD fibroblasts in response to TGF-β (Fig. 4B). Notably, *Mfap5* expression displayed a trend toward upregulation in response to TGF-β stimulation but did not reach statistical significance (Fig. 4F).

Since our data showed that some of the functions controlled by RAS-PI3K in CAFs were dependent on YAP activity, we next wondered whether glycoprotein expression was mediated through YAP-dependent mechanisms. Treatment of WT CAFs with verteporfin showed that while the expression of Igsf10 in verteporfin-treated fibroblasts closely resembled those observed in RBD cells, this similarity was not consistent across most glycoproteins. Notably, the magnitude of downregulation or upregulation observed in verteporfin-treated cells was often distinct from that detected in RBD

fibroblasts (Fig. 4F). These results suggest that the transcriptional changes observed in RBD fibroblasts are not fully explained by YAP-dependent mechanisms.

We next searched in our initial RNA-seq data (Supplementary Table S4) to identify glycosylation enzymes with altered expression that could explain the differences in the glycosylation pattern found in RBD-derived matrices. Among the most significantly deregulated genes, we focused on A4Galt, Galnt13, Galnt17, Glt1d1, and St6galnac2, all of which have been previously implicated in the glycosylation of ECM components. qPCR validation confirmed a significant downregulation of these enzymes in RBD fibroblasts, both under TGF-β stimulation and in response to conditioned medium from KRAS-mutant KPB6 cells (Fig. 4G). These findings are consistent with the observed alterations in glycoprotein content and suggest that impaired glycosylation processes may contribute to the ECM defects induced by RAS-PI3K disruption. We also treated WT fibroblasts with verteporfin and assessed gene expression level of the same glycosylases by qPCR. Similar to glycoproteins, verteporfin treatment failed to recapitulate the downregulation observed in RBD fibroblasts, indicating that the regulation of these glycosylation enzymes is largely independent of YAP (Fig. 4G).

To assess the clinical relevance of these findings, we analyzed patient datasets using KMplotter[54] tool to determine whether the expression of glycoproteins altered in RBD fibroblasts correlated with survival outcomes in lung adenocarcinoma. Interestingly, the overexpression of several glycoproteins that were upregulated in RBD-derived matrices, including Aebp1, Efemp2, Fbn1, Matn2, and Mgp, was associated with improved prognosis. Conversely, downregulation of Mfap5, which was also decreased in RBD fibroblasts, correlated with better survival outcomes (Supplementary Fig. S4C).

CDMs Produced by RBD CAFs Impact Tumor Cell Behavior

The data presented thus far demonstrate that RAS-PI3K disruption profoundly alters ECM composition, structure, and mechanical properties, resulting in matrices that are less organized, thinner, and softer. Given the central role of the ECM in regulating tumor cell behavior, these findings raise the question of whether the altered ECM generated by RBD CAFs impacts tumor cell phenotype and function.

To address this, we investigated how the KRAS-mutant lung tumor cell lines KPB6 and LKR13 behave when seeded on the decellularized CDMs produced by WT or RBD CAFs.

The morphology and arrangement of the tumor cells was strikingly different depending on the underlying matrix. Tumor cells seeded on WT CDMs exhibited an elongated phenotype, aligned along a common axis, forming end-to-end arrangements. In contrast, cells cultured on RBD CDMs appeared more rounded and retained cell-cell junctions (Fig. 5A and Supplementary Fig. S5A). Quantitative analysis of KPB6 cells seeded on RBD CDMs displayed significantly higher circularity compared to those on WT CDMs (Supplementary Fig. S5B).

We next observed that the organization of ECM fibers dictated tumor cell alignment and cytoskeletal arrangement. Immunofluorescence staining of fibronectin fibers within the ECM and actin filaments in tumor cells revealed a strong correlation between the alignment of matrix fibers and the cytoskeletal orientation of both KPB6 and LKR13 cells (Fig. 5B and supplementary Fig. S5C).

To further investigate how ECM remodeling affects tumor cell organization and behavior, we examined the formation and orientation of focal adhesions in KPB6 cells reseeded on matrices produced by WT-, RBD-, p110α-rescued, and alpelisib-treated CAFs. KPB6 cells cultured on WT matrices established large, well-defined focal adhesions that showed higher degree of alignment with the direction of fibronectin fibers, and presented higher contact points with the fibers as indicated in co-localization analysis (Fig. 5C and Supplementary Fig. S5D). In contrast, cells seeded on RBD matrices displayed more disorganized focal adhesions with significant changes in alignment and co-localization with the underlying ECM fibers, often forming perpendicular-to-fiber direction and showing decreased contact points with ECM fibers (Fig. 5C and Supplementary Fig. S5D). Importantly, reintroducing functional p110α into RBD CAFs partially restored focal adhesion alignment. Conversely, treating WT CAFs with alpelisib phenocopied the defects observed in RBD matrices (Fig. 5C and Supplementary Fig. S5D).

The differences in tumor cell morphology and organization prompted us to examine whether these phenotypic changes were associated with alterations in epithelial-to-mesenchymal transition (EMT) programs. Gene expression analysis revealed a significant reduction in EMT-promoting transcription

factors and markers, including *Snail1*, *ZEB*, *Twist*, N-*Cadherin*, and *Vimentin*, in KPB6 and LKR13 cells cultured on RBD-derived matrices compared to WT-derived matrices (Fig. 5D and Supplementary Fig. S5E). In contrast, the expression of *E-Cadherin*, a hallmark of epithelial state, was significantly upregulated in tumor cells reseeded on RBD-derived CDMs (Fig. 5E). Immunofluorescence analysis of KPB6 cells further confirmed a marked increase in E-Cadherin protein levels when seeded in RBD derived CDMs (Fig. 5F).

Together, these findings suggest that the ECM generated by RBD CAFs promotes a more epithelial-like phenotype in tumor cells, which is generally associated with reduced migratory and invasive potential [55, 56]. Consistent with this hypothesis, random migration assays revealed that KPB6 cells seeded on RBD-derived matrices exhibited a modest but significant reduction in migration compared to those cultured on WT-derived matrices (Supplementary Fig. S5F).

Finally, we evaluated the impact of CDMs on tumor cell proliferation. KPB6 and LKR13 cells were seeded onto decellularized matrices produced by WT, RBD, p110α-rescued RBD CAFs, and alpelisib-treated WT CAFs. Proliferation assays revealed that tumor cells grown on RBD-derived matrices exhibited a marked reduction in proliferation compared to those grown onto WT CDMs (Fig. 5G and Supplementary Fig. S5G). Culture in matrices produced by RBD CAFs with reintroduced functional p110α partially restored tumor cell proliferation. Similarly, matrices from Alpelisib-treated WT CAFs reduced tumor cell proliferation to levels comparable to those observed on RBD-derived matrices (Fig. 5G and Supplementary Fig. S5G).

We also analyzed the behavior of tumor cells seeded on ECM generated by human CAFs. Given that matrices produced by CAFs treated with alpelisib were thinner and exhibited less aligned fibers, we hypothesized that these structural alterations might similarly influence tumor cell behavior. To test this, the human lung adenocarcinoma cell line A549 was reseeded onto decellularized matrices produced by human CAFs treated with alpelisib. Consistent with the murine data, A549 cells seeded on matrices generated by untreated CAFs exhibited an elongated morphology and aligned along ECM fibers. In contrast, cells grown on matrices derived from alpelisib-treated CAFs retained more cell-cell

junctions and adopted a less elongated, more epithelial-like morphology, indicative of reduced migratory capacity (Fig. 5H).

Correlation analysis of the alignment of actin cytoskeletal filaments in A549 cells relative to the orientation of fibronectin fibers in the matrix confirmed that the cytoskeletal organization of A549 cells closely followed the direction of matrix fibers, mirroring the alignment patterns observed in the murine system (Supplementary Fig. S5H).

Finally, proliferation assays revealed that A549 cells proliferated slowly when reseeded onto matrices derived from alpelisib-treated CAFs compared to those generated by untreated CAFs, further supporting the idea that RAS-PI3K signaling regulates ECM properties that influence tumor cell behavior in both murine and human systems (Fig. 5I).

Fibroblast-Specific Disruption of RAS-PI3K Signaling Reduces Tumor Burden and ECM Deposition in KRAS-Driven Lung Cancer

To directly evaluate the contribution of fibroblast-specific RAS-PI3K signaling to tumor progression, we generated a new mouse model in which Cre recombinase expression is driven by the *Col1a2* promoter, enabling the targeted disruption of RAS-PI3K interaction exclusively in fibroblasts (*Pik3ca*$^{fRBD/flox}$). The *Pik3ca*$^{fRBD/flox}$ model was crossed with KRAS^{LA2} mice, and lung tumors were allowed to develop. At 12 weeks of age, mice were treated with tamoxifen via oral gavage to induce recombination and eliminate RAS-PI3K interaction in fibroblasts. Lungs were harvested and analyzed 16 weeks later to assess tumor burden and ECM remodeling. Gross examination of lung surfaces revealed a significant reduction in the number of visible tumors in *Pik3ca*$^{fRBD/-}$ mice compared to their *Pik3ca*$^{fWT/-}$ counterparts (Supplementary Fig. S6A). Histopathological analysis of H&E-stained lung sections further confirmed a marked decrease in overall tumor burden in the fibroblast-specific RAS-PI3K knockout model (Supplementary Fig. S6B). These findings demonstrate that disrupting RAS-PI3K signaling in fibroblasts is sufficient to impair tumor growth *in vivo*.

To further characterize the impact of fibroblast-specific RAS-PI3K disruption, we analyzed markers of tumor cell proliferation and found that phosphorylated histone H3 (p-HH3) was significantly reduced

in proliferating tumor cells within *Pik3ca*$^{fRBD/-}$ lungs, consistent with the previously observed defects in CAF-driven ECM remodeling and reduced tumor cell proliferation *in vitro* (Supplementary Fig. S6C). We next assessed markers of CAF activation and ECM deposition. Immunostaining for α-SMA demonstrated a significant decrease in the number of activated fibroblasts in *Pik3ca*$^{fRBD/-}$ tumors (Supplementary Fig. S6C), leading us to conclude that RAS-PI3K signaling is required to sustain CAF activation. Consistent with this, fibronectin staining revealed a pronounced reduction in ECM deposition in *Pik3ca*$^{fRBD/-}$ tumors compared to controls (Supplementary Fig. S6C). Collagen deposition, assessed by Sirius Red staining, was also diminished in *Pik3ca*$^{fRBD/-}$ tumors, mirroring the defects in ECM remodeling observed *in vitro* (Supplementary Fig. S6C).

To evaluate whether the impact of RAS-PI3K disruption in CAFs extends to more aggressive tumor models, we used an orthotopic model in which KRAS-mutant KPB6 lung cancer cells were tail vein-injected into tamoxifen treated *Pik3ca*$^{fRBD/-}$ and control mice; this model forms adenocarcinomas, unlike the KRAS^{LA2} model which predominantly develops adenomas. Lungs were harvested 21 days after tumor cell injection for analysis. Histological examination with H&E staining and quantification of tumor burden revealed that deletion of RAS-PI3K specifically in fibroblasts caused a significant reduction in tumor growth (Fig. 6A). Importantly, in the absence of tamoxifen administration, no differences in tumor burden were observed between groups, confirming that the observed effects were dependent on the fibroblast-specific deletion of RAS-PI3K.

Consistent with the observed reduction in tumor burden, mice with fibroblast-specific RAS-PI3K deletion exhibited a significant increase in survival compared to controls (Fig. 6B). Although the differences were relatively modest, it remains biologically and statistically significant given the highly aggressive nature of this model (30 days of median survival in the control group compared with 350 days in the KRAS^{LA} model[39]).

To further investigate the effects of fibroblast-specific RAS-PI3K deletion in tumor growth and tumor ECM remodeling, we first analyzed tumor cell proliferation using IHC staining for p-HH3. Consistent

with the effects observed in the genetic model, fibroblast-specific deletion of RAS-PI3K led to a significant reduction in the number of proliferating cells (Fig. 6C and 6D). We next examined whether ECM remodeling and CAF activity were similarly affected. Immunostaining revealed a marked reduction in the number of α-SMA-positive CAFs in tumors from *Pik3ca*$^{fRBD/-}$ mice, along with a significant decrease in collagen deposition, as measured by Sirius Red staining, and fibronectin levels (Fig. 6C and 6D). Alcian Blue staining on sections of the orthotopic tumors confirmed that tumors from *Pik3ca*$^{fRBD/-}$ mice exhibited a dramatic reduction in glycosylation levels compared to controls (Fig. 6C and 6D), as indicated in the matrisome analysis.

Given the critical role of the ECM in modulating drug sensitivity [57, 58], we hypothesized that the changes caused in the ECM of the *Pik3ca*$^{fRBD/flox}$ model might enhance therapeutic efficacy. Both *Pik3ca*$^{fRBD/-}$ and control mice were treated with cisplatin and pemetrexed, a standard-of-care combination for patients with lung adenocarcinoma. Remarkably, fibroblast-specific deletion of RAS-PI3K significantly improved the response to treatment, with *Pik3ca*$^{fRBD/-}$ mice exhibiting an averaged 60% reduction in tumor burden compared to untreated *Pik3ca*$^{fRBD/-}$ mice, while control mice showed only a 35% reduction under the same treatment conditions (Fig. 6E and F).

We next examined whether the enhanced treatment response observed in *Pik3ca*$^{fRBD/-}$ mice also extended to targeted therapies. Mice were treated with RMC-7977, a RAS(ON) multi-selective tri-complex inhibitor targeting the full spectrum of oncogenic RAS(ON) proteins. Consistent with our findings with chemotherapy treatment, the reduction in the size of tumors in *Pik3ca*$^{fRBD/-}$ mice was significantly greater (78%) than in control mice (68%) following RMC-7977 treatment (Fig. 6E).

DISCUSSION

In this study, we have demonstrated that fibroblast-specific disruption of RAS-PI3K signaling profoundly alters the tumor microenvironment by impairing CAF activation, ECM remodeling, and tumor-supportive functions. Through a comprehensive and integrated approach that includes proteomic, genomic, molecular, genetic, and pharmacological strategies, as well as specialized mouse models, we show that the ECM alterations caused by disruption of RAS-PI3K interaction in CAFs not only suppress tumor growth and burden but also enhance sensitivity to both standard chemotherapy and targeted therapies. These results underscore the importance of fibroblast-specific signaling pathways in shaping tumor progression and highlight the therapeutic potential of targeting ECM-regulatory mechanisms to improve treatment efficacy.

Our data clearly demonstrate that RAS-PI3K signaling is required for the acquisition of a myoCAF phenotype, characterized by the expression of α-SMA, cytoskeletal remodeling, and ECM contractility. PI3K activity plays a central role in controlling actin cytoskeleton dynamics, contractility, and focal adhesion formation[59-62], processes that are fundamental for CAF activation and ECM remodeling[41, 42]. Actin cytoskeleton remodeling not only supports fibroblast contractility, enabling collagen gel contraction and ECM reorganization, but also facilitates mechanotransduction, allowing CAFs to sense and respond to changes in the mechanical properties of their environment[63-66]. In our study, the disruption of RAS-PI3K signaling impaired actin filament organization, ultimately compromising their ability to generate tension and remodel the ECM. The defects in filamentous actin were closely mirrored by pharmacological inhibition of PI3K and, in some cases, by YAP inhibition, highlighting the functional connection between cytoskeletal dynamics and ECM remodeling.

CAFs are a highly heterogeneous population, exhibiting diverse phenotypes, including tumor-promoting, immune-modulating, and even tumor-restraining phenotypes[1, 6, 7, 67, 68]. While our results demonstrate that RAS-PI3K signalling is required for the acquisition of a myoCAF phenotype, it remains unclear whether all CAF subsets rely equally on RAS-PI3K signaling to support their functions. Future studies should address whether specific CAF subpopulations are more dependent on RAS-PI3K

signaling and whether targeting this pathway preferentially reprograms certain subsets while sparing others. Such insights could have important implications for developing more precise and effective therapeutic strategies, particularly in tumors where CAF heterogeneity may contribute to differential responses to treatment.

YAP has been widely described as a mechanosensitive transcriptional regulator that integrates extracellular and intracellular cues to modulate cytoskeletal organization and ECM remodeling[44, 46, 69]. Consistent with this role, we show that loss of RAS-PI3K impairs YAP transcriptional activity, leading to selective alterations in YAP target genes associated with ECM production and contractility. However, we also find that several transcriptional and ECM-related changes observed in RAS-PI3K-deficient CAFs occur independently of YAP, highlighting the complexity of RAS-PI3K-mediated regulation. This dual mechanism—partly dependent and partly independent of YAP—represents a novel layer of control over CAF biology, raising the possibility that additional signaling pathways converge with RAS-PI3K to drive ECM remodeling.

The effects of RAS-PI3K disruption extend beyond gene expression to functional and structural alterations in ECM production and organization. Our study demonstrates that RAS-PI3K signaling in CAFs plays a pivotal role in shaping the tumor microenvironment by coordinating multiple aspects of ECM remodeling and stromal dynamics. ECM remodeling driven by CAFs also affects the sequestration and release of growth factors, such as TGF-β, VEGF, and FGF, among others, which are embedded in the matrix[70, 71]. The disruption of ECM structure observed in RAS-PI3K-deficient CAFs could alter growth factor gradients and signaling dynamics, potentially influencing tumor proliferation and metastatic seeding. This raises the possibility that ECM-targeting therapies may also modulate paracrine signaling pathways that support tumor progression[9, 19]. Investigating how changes in ECM composition influence growth factor availability could provide further insights into the mechanisms driving the observed therapeutic responses and identify additional vulnerabilities within the microenvironment.

The alterations introduced by RAS-PI3K disruption in CAFs culminate in the generation of a microenvironment that is less oncogenic, as evidenced by reduced tumor proliferation and EMT markers observed *in vitro*, along with diminished tumor burden and increased survival *in vivo*. Importantly, these findings extend beyond murine models, as we demonstrate that pharmacological inhibition of PI3K in human CAFs produces similar ECM defects, highlighting the conserved nature of this pathway across species. The reduced fibronectin alignment, collagen deposition, and glycoprotein content observed upon RAS-PI3K disruption are consistent with features associated with less aggressive tumor phenotypes across multiple cancer types [72-79]. For example, disorganized and softer ECMs are often linked to reduced metastatic potential and improved patient prognosis, while aligned and stiff matrices promote invasion and resistance to therapy[80-83].

The clinical relevance of these findings is underscored by survival analyses in patients with lung adenocarcinoma, which revealed that the expression of several glycoproteins dysregulated in RAS-PI3K-deficient CAFs correlates with better prognoses. This further points to ECM alterations induced by RAS-PI3K disruption creating a less permissive microenvironment for tumor progression, potentially limiting tumor cell invasiveness and metastatic potential. Given the well-established role of ECM composition and organization in modulating key tumor-promoting processes, including migration, proliferation, and chemoresistance[8, 84-86], these results suggest that targeting stromal signaling pathways may complement existing cancer therapies[14, 70].

Notably, our *in vivo* data demonstrate that fibroblast-specific RAS-PI3K disruption enhances the efficacy of both standard chemotherapy (cisplatin and pemetrexed) and targeted therapies (RMC-7977), leading to greater reductions in tumor burden and improved animal survival even in a highly aggressive orthotopic tumor model. A remaining question that warrants further investigation is whether pharmacological inhibition of p110α or other downstream effectors in CAFs could serve as an adjuvant strategy to enhance treatment responses in lung adenocarcinoma and potentially other stromal-rich tumor types. The observed synergy between RAS-PI3K disruption and chemotherapy or targeted therapies suggests that targeting stromal signaling pathways could complement standard

treatments not only by limiting tumor-supportive ECM properties but also by normalizing the microenvironment, potentially enhancing immune infiltration and improving drug delivery[87, 88]. This raises the exciting possibility that therapies simultaneously targeting tumor-intrinsic and stromal-dependent mechanisms may achieve more durable responses in cancer patients.

While our study focuses on the role of RAS-PI3K signaling in CAFs and its direct impact on tumor cell behavior, it remains possible that the effects of RAS-PI3K disruption in CAFs extend to the functionality of other components of the tumor microenvironment. Changes in ECM structure and composition have been linked to vascular remodeling and angiogenesis[89-92] as well as to immune cell recruitment and activation[57, 93, 94], potentially shaping tumor progression and therapeutic responses. Whether the RAS-PI3K pathway indirectly modulates these processes through its effects on CAFs or acts through parallel mechanisms warrants further investigation.

Given the prevalence of KRAS mutations in lung adenocarcinoma, we have focused on lung cancer driven by this oncogene, leveraging the availability of genetically engineered mouse models that recapitulate key aspects of the disease and well-established models to investigate the impact of RAS-PI3K signaling in CAFs. However, the effects of RAS-PI3K disruption in CAFs may extend to lung tumors driven by alternative oncogenic drivers, such as EGFR mutations or ALK fusions. Additionally, since many solid tumors, including pancreatic ductal adenocarcinoma (PDAC) and triple-negative breast cancer (TNBC), are characterized by desmoplastic stroma and extensive ECM remodeling[57, 95-98], it is plausible that targeting RAS-PI3K signaling in CAFs may have broad therapeutic relevance. Testing whether PI3K inhibition normalizes these stromal properties in diverse tumor types could uncover broader vulnerabilities and identify patient populations most likely to benefit from this approach.

Our findings highlight the critical role of RAS-PI3K signaling in shaping the tumor microenvironment, challenging the initial view that RAS activity in tumor progression is primarily confined to cancer cells. While the oncogenic effects of RAS signaling within tumor cells have been extensively characterized[23, 96, 99-103], our study reveals that RAS-PI3K also exerts profound effects on stromal components,

particularly CAFs, to orchestrate ECM remodeling and microenvironmental dynamics. By demonstrating that disruption of RAS-PI3K signaling in fibroblasts impairs ECM production, collagen crosslinking, and mechanotransduction, we underscore the broader influence of RAS effectors in sustaining the structural and functional properties of the tumor stroma.

These findings not only position RAS-PI3K signaling as a key regulator of CAF behavior but also raise the possibility that other RAS effector pathways, including MAPK and RAL-GTPases, may similarly influence microenvironmental remodeling. Given the complexity of stromal-tumor interactions, it is likely that RAS signaling operates through multiple parallel mechanisms to fine-tune ECM composition, stiffness, and organization, thereby modulating tumor cell behavior and therapeutic responses. Our work provides new insights into how oncogenic pathways extend their influence to shape the tumor microenvironment and suggest that targeting stromal RAS-PI3K activity, either alone or in combination with therapies targeting cancer cells, may represent a novel strategy to disrupt tumor-stromal crosstalk, normalize the ECM, and limit tumor aggressiveness to improve treatment outcomes.

ACKNOWLEDGEMENTS

This work was supported by grants from the Spanish Ministry of Science and Innovation (RTI2018-099161-A-I00 and CPP2022-009780), Rosetrees Trust, AECC Excellence program Stop Ras Cancers (EPAEC222641CICS), Programa JAE-Intro ICU from CSIC (JAEICU-21-IBMCC-6) and JCyL (CSI185-20). This research was co-financed by FEDER funds. The CIC is supported by the Programa de Apoyo a Planes Estratégicos de Investigación de Estructuras de Investigación de Excelencia of Castilla y León autonomous government (CLC-2017-01). The authors wish to thank the Pathology Unit, the Mouse Model Experimentation Unit, and the Advanced Cellular Analysis Unit at CIC for their assistance in carrying out this work. The authors thank members of the lung TRACERx consortium whose study derived the human cancer-associated fibroblasts (CAFs) that were used in this study. The TRACERx study is funded by Cancer Research UK (CRUK; C11496/A17786) and the creation of TRACERx patient-derived models was supported by the Wellcome Trust (209199/Z/17/Z), the CRUK Lung Cancer Centre of Excellence and the Francis Crick Institute, which receives its core funding from CRUK (FC001169), the MRC (FC001169), and the Wellcome Trust (FC001169). The authors also acknowledge Revolution Medicines for providing RMC-7977.

MATERIALS AND METHODS

Mouse model generation and experimental procedures

Generation of the mouse model with fibroblast-specific RAS-PI3K disruption were generated by crossing *Pik3ca*$^{RBD/flox}$ mice [35] with Tg(Col1a2-cre/ERT,-ALPP)7Cpd/J (The Jackson Laboratory; referred to here as *Col1a2-CreER*). For tumor studies, this model was further bred with KRAS^{LA2} mice[39].

For the generation of the orthotopic model of lung cancer, 1x10^{5} KPB6 tumor cells were injected through the tail vein of *Pik3ca*$^{fRBD/-}$ mice in a total volume of 100 µl PBS.

For tumor growth experiments, mice were sacrificed 21 days post-injection, and lungs were collected for histological analysis. For survival studies, mice were monitored daily and euthanized upon reaching humane endpoints, including a 20% reduction in body weight relative to the starting weight or signs of respiratory distress, as per approved ethical guidelines. For therapeutic studies, drug treatments began 1 week after tail vein injection.

All animals were housed and maintained at the NUCLEUS animal facility of the University of Salamanca under standard pathogen-free conditions. Animal care and experimental procedures were conducted in strict compliance with European (2007/526/CE) and Spanish (RD 1201/2005; RD 53/2013) legislation, and the study was approved by the Bioethics Committee of the Cancer Research Center.

Efforts were made to minimize animal suffering, and humane endpoints were established in accordance with the approved protocols. Animals were randomly assigned to experimental groups to ensure unbiased allocation, with group sizes balanced based on birth dates. Researchers were blinded to group assignments during data collection and analysis to reduce bias. No formal sample size calculation was performed; however, sample sizes were determined based on prior experience and feasibility. Pre-established inclusion and exclusion criteria were applied to maintain experimental integrity. Animals presenting pre-existing health conditions were excluded, and no gender restrictions were imposed in this study.

In Vivo Tamoxifen and Drug Treatments

Mice were treated with tamoxifen (3.2mg, dissolved in 80 µL of corn oil (MedChemExpress)) by oral gavage for 3 consecutive days. For long-term experiments, tamoxifen administration was repeated once every 2 weeks throughout the duration of the study to maintain Cre recombination efficiency.

Cisplatin/Pemetrexed treatment were administered intraperitoneally twice a week for 2 consecutive weeks. RMC-7977 was administered by oral gavage 5 days per week for 2 consecutive weeks. Mice received either vehicle, cisplatin (3 mg/kg/day; MedChemExpress), pemetrexed (100 mg/kg/day; MedChemExpress), or RMC-7977 (10 mg/kg/day). RMC-7977 was provided by Revolution Medicines. Cisplatin and pemetrexed were dissolved NaCl 0.9%, while RMC-7977 was prepared as previously described[101].

Tissue culture

Cells were cultured in Dulbecco's Modified Eagle Medium (DMEM; (Gibco)) supplemented with 10% fetal bovine serum (FBS; (Gibco)), 100 U/mL penicillin, 100 µg/mL streptomycin (Pen/Strep; (Gibco)) and 1% glutamine. Cells were maintained in a humidified incubator at 37°C with 5% CO2.

Murine embryonic fibroblasts (MEFs) were activated with 10 ng TGF-β1 (PeproTech) for 24 hours or treated with conditioned medium (CM) from the KRAS-mutant lung cancer cell lines KPB6 and LKR13. CM were prepared by culturing 1.5×10^6 cancer cells in DMEM + 5% FBS for 48 hours, followed by filtration through a 0.45 µm filter. Fibroblasts were incubated with CM for 24 hours.

Human CAF (hCAF) cultures were explanted from tumor tissue from patients with lung adenocarcinoma within the Tracking Cancer Evolution through Therapy (TRACERx) clinical study (REC reference 13/LO/1546). hCAFs were activated similarly to murine CAFs using conditioned medium from A549 cells.

CDM generation and decellularization

Tissue culture dishes were coated with 1 mL of 0.2% gelatin solution (Sigma) and incubated at 37°C for 1 hour. For dishes of different sizes, reagent volumes were adjusted accordingly. After incubation, the gelatin solution was aspirated, and the dishes were rinsed with DPBS+ (PBS + 1mM $CaCl_2$ + 1mM $MgSO_4$). To cross-link the gelatin, 1 mL of 1% glutaraldehyde solution (Sigma) (prepared in DPBS+) was

added to each dish and incubated at room temperature for 30 minutes. The dishes were then washed three times with 1 mL of DPBS+ for 5 minutes each to remove any excess glutaraldehyde. Free aldehyde groups were next blocked adding 1 mL of 1 M ethanolamine (Sigma) to each dish, followed by a 30-minute incubation at room temperature. This was followed by three additional washes with DPBS+. Dishes prepared in this manner were stored at 4°C under sterile conditions for up to 3 days before use.

8.5×10^4 TGF-b activated MEFs or $1x10^5$ hCAFs activated with conditioned medium of lung cancer cell line A549 (CM-A549) were seeded into each 35 mm dish containing 1 mL of culture medium and cultured for 24 hours to allow for cell attachment. Following initial attachment, the culture medium was replaced with fresh matrix medium (DMEM+10 ng TGF-β for MEFs or CM-A549 for hCAFs supplemented with 50 µg/mL ascorbic acid) (Sigma) to enhance collagen synthesis. The medium was partially replaced every 48 hours with fresh matrix medium containing 100 µg/mL ascorbic acid and 20 ng TGF-β (MEFs) to maintain a final concentration of 50 µg/mL and 10ng respectively in the culture. This process was continued for 7-9 days, depending on the fibroblast cell type used, to ensure adequate matrix deposition.

To remove cells from the deposited matrix (decellularization), the culture medium was carefully aspirated, and the dishes were gently rinsed twice with 2 mL of DPBS− (PBS lacking $CaCl_2$ and $MgSO_4$), ensuring that the pipette tip was placed against the dish wall to avoid disturbing the matrix and cells at the bottom. Following rinsing, 0.5 mL of pre-warmed (37°C) extraction buffer (DPBS- + 1% Triton X-100 (Sigma) + 20mM NH_4OH (Honeywell)) was gently added. Cell lysis was monitored using an inverted microscope, with incubation continuing at 37°C until no intact cells were observed. Cellular debris was removed by slowly adding 2 mL of DPBS− to the dishes. The dishes were then stored overnight at 4°C in DPBS− to further stabilize the matrix.

The next day, diluted cellular debris was cautiously aspirated using a pipette, ensuring that the liquid layer covering the matrix was not completely removed, thus keeping the matrix hydrated. This wash step was repeated by gently adding another 2 mL of DPBS− and aspirating, followed by two additional

washes with DPBS+, being careful to avoid creating turbulence. To minimize DNA debris, the matrices were treated with DNase I (Roche) by adding 1 mL of the enzyme solution and incubating for 30 minutes at 37°C. After incubation, the DNase I solution was aspirated, and the matrices were washed twice with 2 mL of DPBS+. The matrix-coated plates or coverslips were then covered with at least 3 mL of DPBS-. These were sealed with Parafilm® and stored at 4°C until used. For signal transduction assays, matrices were stored in serum-free medium.

For the generation of CDMs by fibroblasts in coculture with cancer cells, plates were coated with gelatin, and fibroblasts were seeded as described previously, without prior activation with TGF-β1. The following day, 6×10^5 KPB6 or LKR13 cancer cells were seeded onto the fibroblasts. After 24 hours, the culture medium was replaced with fresh matrix medium (DMEM supplemented with 50 µg/mL ascorbic acid). Medium was partially replaced every 48 hours with fresh matrix medium containing 100 µg/mL ascorbic acid, maintaining a final concentration of 50 µg/mL ascorbic acid in the culture. After 8 days, non-decellularized CDMs were fixed for subsequent immunofluorescence analysis.

Mass spectrometry

Proteomics experiments were performed using mass spectrometry as previously reported[104-106] with some technical modifications. Peptides, digested from proteins using trypsin, were desalted with the AssayMAP Bravo (Agilent Technologies) platform using the peptide clean-up v3.0 protocol. Briefly, reverse phase S cartridges (Agilent, 5 µL bed volume) were primed with 250 µL 99.9% acetonitrile (ACN) with 0.1%TFA and equilibrated with 250 0.1% TFA at a flow rate of 10 µL/min. The samples were loaded at 20 µL/min, followed by an internal cartridge wash with 0.1% TFA at a flow rate of 10 µL/min. Peptides were then eluted with 105 µL of solution (70/30 ACN/ H2O + 0.1% TFA. Eluted peptide solutions were dried in a SpeedVac vacuum concentrator and peptide pellets were stored at −80 °C.Dried peptides were dissolved in 0.1% TFA and analysed by nanoflow ultimate 3000 RSL nano instrument was coupled on-line to a Q Exactive plus mass spectrometer (Thermo Fisher Scientific). Gradient elution was from 3% to 28% solvent B in 90 min at a flow rate 250 nL/min with solvent A being used to balance the mobile phase (buffer A was 0.1% formic acid in water and B was 0.1% formic

acid in acetonitrile). The spray voltage was 1.95 kV and the capillary temperature was set to 255 ºC. The Q-Exactive plus was operated in data dependent mode with one survey MS scan followed by 15 MS/MS scans. The full scans were acquired in the mass analyser at 375- 1500m/z with the resolution of 70 000, and the MS/MS scans were obtained with a resolution of 17 500. MS raw files were converted into Mascot Generic Format using Mascot Distiller (version 2.8.1) and searched against the SwissProt database (SwissProt_2021_02.fasta) restricted to human entries using the Mascot search daemon (version 2.8.0). Allowed mass windows were 10 ppm and 25 mmu for parent and fragment mass to charge values, respectively. Identified peptides were quantified using in-house software Pescal as described before[107, 108]. The resulting quantitative data was parsed into R (Version 4.2.2) for further normalisation and statistical analysis. The code used in analysis and visualization of data is available at https://github.com/CutillasLab/protools2.

Phosphoproteomics experiments were performed using mass spectrometry as previously reported [105, 109]. In brief, frozen tissues were grounded and lysed in 8M urea buffer and supplemented with phosphatase inhibitors (10 mM Na_3VO_4, 100 mM β-glycerol phosphate and 25 mM $Na_2H_2P_2O_7$ (Sigma)). Proteins were digested into peptides as outlined above. Phosphopeptides were enriched from total peptides by TiO2 chromatography essentially as reported previously[110]. Dried phosphopeptides and peptides were dissolved in 0.1% TFA and analysed by LTQ-Orbitrap XL mass spectrometer (Thermo Fisher Scientific) connected to a nanoflow ultra-high-pressure liquid chromatography (UPLC, NanoAcquity, Waters). Peptides were separated using a 75 µm × 150 mm column (BEH130 C18, 1.7 µm Waters) using solvent A (0.1% FA in LC–MS grade water) and solvent B (0.1% FA in LC–MS grade ACN) as mobile phases.

The UPLC settings consisted of a sample loading flow rate of 2 µL/min for 8 min followed by a gradient elution with starting with 5% of solvent B and ramping up to 35% over 220 min for total proteomics and 100 min gradient for phosphoproteomics followed by a 10 min wash at 85% B and a 15 min equilibration step at 1% B. The flow rate for the sample run was 300 nL/min with an operating back pressure of about 3800 psi. Full scan survey spectra (m/z 375–1800) were acquired in the Orbitrap

with a resolution of 30000 at m/z 400. A data dependent analysis (DDA) was employed in which the five most abundant multiply charged ions present in the survey spectrum were automatically mass-selected, fragmented by collision-induced dissociation (normalized collision energy 35%) and analysed in the LTQ. Dynamic exclusion was enabled with the exclusion list restricted to 500 entries, exclusion duration of 30 s and mass window of 10 ppm.

MASCOT search was used to generate a list of proteins. Peptide identification was by searchers against the SwissProt database (version 2013-2014) restricted to human entries using the Mascot search engine (v 2.5.0, Matrix Science, London, UK). The parameters included trypsin as digestion enzyme with up to two missed cleavages permitted, carbamidomethyl (C) as a fixed modification and Pyro-glu (N-term), Oxidation (M) and Phospho (STY) as variable modifications. Datasets were searched with a mass tolerance of ±5 ppm and a fragment mass tolerance of ±0.8 Da. Label-free quantification was carried out with Pescal as outline above.

Phosphoproteomic Data Processing and Analysis

Data normalization, log2 transformation, and standardization were performed for downstream analysis. Sample similarity was evaluated using Spearman correlation and principal component analysis (PCA), leading to the exclusion of outliers. Differentially phosphorylated proteins were identified using a t-test, with BH method applied for multiple testing. Proteins with a p-value < 0.05 and an absolute log2 fold change > 1 were considered significantly differentially phosphorylated. Functional enrichment analysis on Gene Ontology (GO)[111] and Kyoto Encyclopedia of Genes and Genomes (KEGG)[112] were conducted using the clusterProfiler (v4.10.0)[113] package in R (v4.3.2). Additionally, kinase enrichment analysis for the differentially phosphorylated proteins was performed using the Kinase Library[114]. Differentially phosphorylated proteins common to the RBD vs WT and WT+Byl vs WT comparisons were identified, and homologous gene conversion was performed using homologene (v1.4.68.19.3.27) package.

Visualization of volcano plots and expression heatmaps was done using ggplot2 (v3.4.4) and heatmap (v1.0.12), respectively. All the phosphoproteomic data processing, statistical analyses, and visualizations were performed in R.

RNAseq analysis

Gene expression quantification was performed using the Salmon algorithm[115] to achieve transcript-level quantification. Differential expression analysis was conducted with the edgeR R package[116], applying its statistical framework to identify significantly differentially expressed genes. Over-representation analysis was carried out using the clusterProfiler suite of R packages[113, 117] to identify enriched pathways and functional categories.

Collagen gel contraction assays

To assess force-mediated collagen remodeling, 4×10^4 murine CAFs, or 8×10^4 human CAFs (hCAFs), were embedded in µL of Rat tail type I collagen (Corning) solution prepared by mixing collagen stock with 2.5% NaOH (1N) and 16.6 ng TGF-β1 in PBS under sterile conditions at 4ºC. Once the gel was set, cells were maintained in DMEM+10%FBS. Gel contraction was monitored daily by taking photographs of the gels. The gel contraction value refers to the contraction observed after 3 days for murine CAFs or 5 days for hCAFs. Contraction index was calculated as the percentage reduction in gel surface area relative to the initial area using ImageJ software.

Morphological analysis of CDM fibers

Morphological features were extracted from the microscopy images using a pipeline of traditional image processing steps implemented in Matlab© (The Mathworks™, Natick, USA). The original color images were first converted to grayscale and then processed with a Gaussian low-pass filter (filter size = 8, standard deviation = 3) to reduce noise. The filtered image was subtracted from the grayscale image to remove background noise and subsequently thresholded. The thresholded image was morphologically thinned, ensuring each region was reduced to a width of one pixel, and regions of connected pixels were identified and labeled. Regions with a major axis smaller than 20 pixels were excluded from the analysis. For each image, the following morphological metrics were extracted:

number of objects, length, and width of each object. It is important to note that one object does not necessarily correspond to a single fiber. A single fiber may appear as two or more objects if it is broken, or multiple fibers may be merged into a single object if they are intersecting or in close proximity. However, as the average number of objects extracted per image was in the thousands, the extracted metrics can be considered representative of the fibers in the images.

The code used for this analysis is available publicly at the following repository: https://github.com/reyesaldasoro/RBD_Cells. The repository will be made public upon the acceptance of the manuscript.

CDM stiffness

The elastic modulus of matrices produced by fibroblasts was quantitatively evaluated using Atomic Force Microscopy (AFM). Fibroblasts were cultured on cover glass slides, allowing them to synthesize extracellular matrix (ECM) directly on the coverslips. These prepared samples were then placed into a BIO-AFM system, specifically designed for integration with an inverted optical microscope (Nikon TE2000). The BIO-AFM system utilized a V-shaped silicon nitride probe (nominal spring constant k = 0.03 N/m) with a four-sided pyramidal tip (Bruker AFM Probes) to ensure precise force measurements. To minimize localized variability and enhance data representativeness, no more than three measurements were taken from a single field of view for mechanical characterization. For each matrix type, stiffness was determined by analyzing data collected from ten different points, with measurements performed in triplicate. Force-displacement (F vs. z) curves were obtained at each point using an amplitude of 10 µm and a frequency of 1 Hz.

The elastic modulus was derived from the force-displacement curves through analysis using the Hertz model, as previously described[118, 119]. For each point, five force-displacement curves were recorded, maintaining an indentation depth of 500 nm. Finally, the elastic modulus for each fibroblast-derived ECM subpopulation was calculated. This analysis was based on a minimum of fifty measurements per independent sample, with at least three independent matrices analyzed for each condition ($n \geq 3$).

Confocal Microscopy

All measurements were performed on a Leica TCS SP8 confocal laser scanning microscope, using a 1.40 NA 63× objective (HCX PL APO CS2 63/1.40 Oil Leica Microsystems). For focal adhesion directionality and colocalization analyses 1024x1024 images were acquired exciting with a WLL (White Light Laser) at 488 and 568 nm for the fibronectin and focal adhesions respectively with a zoom factor of 2 and images were obtained in the axial plane every 0.3µm focusing on the focal adhesions solely. Directionality analysis was performed at the equatorial plane were lateral focal adhesions were observed in contact with fibrils while Colocalization analysis was performed at the bottom of the cells were focal adhesions and fibrils overlap in the section. Data analysis was performed using Fiji App1 and more specifically using the "Directionality" Plugin for the directionality analysis and JacoP3 Plug in for the colocalization analysis.

Fluorescence Lifetime Imaging Microscopy (FLIM) Analysis

To assess ECM accessibility and binding properties, we employed Fluorescence Lifetime Imaging Microscopy (FLIM) using the molecular rotor dye DCVJ (9-(2,2-Dicyanovinyl)julolidine) (Sigma-Aldrich), which exhibits viscosity-dependent fluorescence lifetimes. A concentration gradient of DCVJ (100 nM–1 µM) was applied to decellularized extracellular matrix (CDM) fibers generated by WT and RBD fibroblasts. FLIM images (512 × 512 resolution) were acquired using a Leica TCS SP8 confocal laser scanning microscope equipped with a 63×/1.40 NA oil-immersion objective (HCX PL APO CS2 63/1.40 Oil Leica Microsystems) and SP8 Falcon Module.

Phasor Analysis

Phasor transformations were performed to map fluorescence decay data from each pixel into a graphical representation, facilitating the analysis of complex, multi-exponential lifetime distributions. The phasor coordinates for each pixel were calculated as follows:

$$g_{i,j}(\omega) = \frac{\int_0^T I_{i,j}(t)\cos(\omega t)\,dt}{\int_0^T I_{i,j}(t)dt}$$

$$s_{i,j}(\omega) = \frac{\int_0^T I_{i,j}(t)\sin(\omega t)\,dt}{\int_0^T I_{i,j}(t)dt}$$

where ω=2πf and f=1/T is the laser repetition rate. The resulting phasors were plotted within the "universal circle," which defines single-exponential decays based on their lifetimes, ranging from τ = 0 at (1,0) to τ = ∞ at (0,0). Mixtures of two components produce phasor points that lie along a straight line connecting the single-component lifetimes, with the position determined by their relative fractional contributions.

Quantitative analysis was performed by defining two single-exponential lifetimes, τ1 = 1.9 ns and τ2 = 0.3 ns, based on control measurements in glycerol. A linear combination model was applied to calculate the fraction of bound versus unbound molecules within ECM fibers using the relative distances from each phasor point to τ1 and τ2. Lineweaver-Burk plots were generated to determine binding constants and relative binding site availability between WT and RBD CDMs.

Western blot analysis

For Western blot analysis, cells were scrapped and lysed in ice-cold RIPA buffer (50 mM Tris-HCl, pH 7.4, 150 mM NaCl, 1% NP-40, 0.5% sodium deoxycholate, 0.1% SDS) supplemented with c0mplete mini protease inhibitor cocktail (Roche). Protein concentrations were determined using the Bradford assay according to the manufacturer's instructions (Biorad). Protein lysates were resolved on 6-18% SDS-PAGE gels (Invitrogen), transferred onto a PVDF membranes and immunoblotted with the indicated primary antibodies (Supplementary Table S6) diluted in 5% bovine serum albumin (BSA; NZYtech) in TBS-Tween (0.1% v/v) overnight at 4°C. Primary antibodies were detected using peroxidase-conjugated

secondary antibodies (Supplementary Table S6), incubated for 1 h at RT in 5% (w/v) non-fat milk in TBS-Tween (0.1% v/v) for 1 hour at room temperature. The protein bands were visualized using an ECL substrate (Cytiva) and visualized on an iBright™ FL1500 (Invitrogen) imaging system.

RNA isolation, Retrotranscription (RT) and quantitative PCR (qPCR)

Total RNA was extracted using the NZY Total RNA Isolation Kit (NZYtech) following the manufacturer's protocol. RNA concentration and quality were assessed with a Nanodrop spectrophotometer. 600 ng of RNA were reverse transcribed into cDNA using the PrimeScript™ RT Reagent Kit (Takara) according to the manufacturer's instructions.

qPCR was performed in triplicate using a QuantStudio™ 5 (384-well block, Thermo Scientific) and PowerTrack SYBR Green Master Mix (Thermo Scientific). Gene expression was normalized to 18S, and relative expression levels were calculated using the $2^{-\Delta\Delta Ct}$ method. Primer sequences are listed in Supplementary Table S7

For gene expression analysis of tumor cells reseeded in decellularized CDMs, 2×10^5 cancer cells were seeded onto CDMs in 6-well plates. RNA was isolated after 6 hours (Snail1, Zeb, Twist) or 24 hours (Vim, N-cadh, E-cadh) as described previously. Prior to RNA isolation, lysates were homogenized using QIAshredder columns (Qiagen).

Proliferation assays in decellularized CDMs

5×10^4 cancer cells were seeded in decellularized CDMs per well in a 24-well plate, at least in triplicates. Proliferation/viability was then assessed at 0, 24 and 48 h using CellTiter-Blue cell viability reagent (Promega). At each timepoint, cells were incubated for 2 h with 50 µCellTiter-Blue solution (added to tissue culture medium), and then fluorescence was measured in a spectrophotometer using 560/590 (excitation/emission) filter settings.

Immnunofluorescence

Cells were fixed in 4% paraformaldehyde (Sigma)/PBS (v/v) for 15 min at RT, and then permeabilized with 0.1% Triton x100 (Sigma-Aldrich)/PBS (v/v) for 5 min at RT, blocked with 3% BSA (w/v) (NZYTech) for 1 h at RT and stained with primary antibodies overnight in humidified chambers at 4°C. Sections

were then washed 3 times with PBS for 5 min, incubated with secondary antibodies and phalloidin, depending on the staining, for 1 h at RT, washed 3 times in PBS for 5 min and mounted using ProLong Gold Antifade reagent with DAPI (Invitrogen). Antibodies references and dilutions are listed in Supplementary Table S6.

For IF of cancer cells reseeded in decellularized CDMs, 1.2×10^5 cancer cells were seeded onto CDMs in 6-well plates. After 24 hours, cells were fixed with 4% PFA at room temperature for 20 minutes. The IF protocol described earlier was followed, except for permeabilization, which was performed with 0.5% Triton X-100 for 10 minutes.

Histology and Analysis

Mice were sacrificed and the lung tissue was immediately removed and fixed overnight in4% PFA. The lungs were transferred to 70% ethanol and processed for paraffin embedding. Tissue sections were cut at 4 µm and were stained with H&E or were immunostained with different antibodies (Supplementary Table S6).

Tumor burden quantification: Lung and tumor area quantifications were carried out on H&E-stained slides. Pictures of each lung lobe were taken on an Olympus Bx51 microscope with a DE74 camera and a 1× objective. Lung and tumor area were measured using ImageJ software.

Phosphohistone H3 (PHH3) quantification: cancer cell nuclei and PHH3+ nuclei were counted using the Fiji multi-point tool. To quantify the proportion of PHH3+ cells in each cancer cell cluster, the number of PHH3/EDU+ were divided by the total number of cells.

α-SMA, Fibronectin, Alcian Blue and Sirius Red quantification: we quantified the positive area divided by the total number of cancer cells in the cluster. For this, we segmented the positive area using an intensity threshold. Cancer cells were counted manually using the Fiji multi-point tool.

Statistical Analysis

Data are presented as mean ± SEM. Significance was determined with GraphPad Prism 10 software using the Student's t test unless stated otherwise.

FIGURE LEGENDS

Figure 1. RAS-PI3K Controls CAF Activation via YAP Signaling and Cytoskeletal Remodeling.

A. Representative images showing the number of α-SMA-positive cells and collagen deposition (Sirius Red staining) in lung tumors with fibroblast-specific RAS-PI3K disruption.

B. Western blot analysis of AKT, RPS6K, and ERK activation in RAS-PI3K-deficient fibroblasts stimulated with TGF-β at the indicated time points.

C. Volcano plot displaying differentially expressed phosphopeptides identified in phosphoproteomic analysis of RAS-PI3K-deficient tumors versus controls. The x-axis represents the log2 fold change (FC) and the y-axis shows the −log10 p-value. Downregulated peptides ($FC \geq 2$, $p < 0.05$) are in blue, upregulated peptides are in red, and non-significant peptides are in grey.

D. Functional enrichment analysis of significantly altered peptides identified in phosphoproteomic profiling of *Pik3ca*$^{RBD/-}$ *vs Pik3ca*$^{WT/-}$ tumors.

E-F. Representative immunofluorescence (IF) images showing α-SMA, vimentin, and YAP expression in WT and RBD fibroblasts in response to TGF-β (E) or conditioned medium (CM) from the KRAS-mutant lung cancer cell line KPB6 (F).

G. Graph showing YAP transcriptional activity assessed by luciferase reporter assays in WT and RBD fibroblasts stimulated with TGF-β or KPB6 CM. Data represent three independent assays. Error bars indicate mean ± SEM; Statistical significance was obtained using t-test: **$p < 0.01$.

H. Circularity analysis of WT and RBD fibroblasts under basal and TGF-β-stimulated conditions, and WT fibroblasts treated with Verteporfin, a YAP inhibitor. Three biological replicates were analyzed (80–100 cells per replicate). Error bars indicate mean ± SEM; Statistical significance was obtained using t-test: *$p < 0.05$; **$p < 0.01$; ***$p < 0.001$; ****$p < 0.0001$; n.s., not significant.

I. Quantification of F-actin content based on phalloidin IF staining in WT and RBD CAFs treated with TGF-β or Verteporfin. Three independent replicates were analyzed (80–100 cells per replicate). Statistical significance was obtained using t-test: *$p < 0.05$; **$p < 0.01$; ***$p < 0.001$; ****$p < 0.0001$; n.s., not significant.

J. Relative gene expression levels of the indicated genes in RBD versus WT fibroblasts (red bars) or WT treated with Verteporfin (green bars) in response to TGF-β activation. Error bars indicate mean ± SEM. Statistical significance was obtained using t-test: *$p < 0.05$; **$p < 0.01$; ***$p < 0.001$; ****$p < 0.0001$.

Figure 2. RAS-PI3K Disruption Alters TGF-β Signaling and ECM-Associated Gene Programs in CAFs.

A. Volcano plot displaying differentially expressed genes identified in the RNAseq analysis RBD vs WT fibroblast and RBD vs WT TGF-β activated CAFs. The x-axis represents the log2 fold change (FC) and the y-axis shows the −log10 p-value. Downregulated peptides (FC ≥ 2, $p < 0.05$) are in blue, upregulated peptides are in red, and non-significant peptides are in grey.

B. Venn diagram showing the overlap of differentially expressed genes identified by RNA-seq in RBD versus WT fibroblasts under basal conditions (purple) and after stimulation with 10 ng TGF-β1 for 24 hours (Green). Numbers indicate unique and shared genes between the two comparisons.

C. Functional enrichment analysis of significantly altered peptides identified in phosphoproteomic profiling of *Pik3ca*$^{RBD/-}$ *vs Pik3ca*$^{WT/-}$ tumors.

Figure 3. RAS-PI3K Signaling is Essential for CAF-Mediated ECM Production and Remodeling.

A. Representative images showing collagen contraction ability of WT, RBD, RBD+p110α, and WT+Alpelisib CAFs and graph showing contraction index quantification. Contraction was performed during 3 days, and values are represented for the 3rd day.

B. Lox and Plod1 relative gene expression levels in RBD versus WT fibroblasts (red bars) or WT treated with Verteporfin (green bars) in response to TGFB or CM activation. Error bars indicate mean ± SEM.

C. Representative images and quantification of length of Sirius Red-stained fibers of CDMs formed by WT, RBD, RBD+p110α, and WT+Alpelisib fibroblasts activated with TGFB.

D. Quantification of the thickness of collagen fibers of CDMs formed by WT, RBD, RBD+p110α, and WT+Alpelisib fibroblasts activated with TGFB.

E. Representative images of collagen fiber content in plugs inserted in the flanks of C57Bl6 mice produced by WT or RBD CAFs.

F. Representative images of fibronectin fiber content in CDMs formed by WT, RBD, RBD+p110α, and WT+Alpelisib fibroblasts activated with TGFB and quantification of the CDM thickness

G. Analysis of fibronectin fiber orientation in CDMs formed by WT, RBD, RBD+p110α, and WT+Alpelisib fibroblasts activated with TGFB.

H. Graph showing stiffness (elastic modulus) of CDMs produced by WT, RBD, RBD+p110α, and WT+Alpelisib fibroblasts activated with TGFB.

I. Representative images of fluorescence lifetime micrographs of different concentrations of DCVJ (200, 300 and 500 nM) staining wild-type (top) and RBD (bottom) CDMs at different concentrations (left). Overlay of the phasors of all samples pointing the bi-exponential behavior of the dye, at τ_1=1.9ns corresponding to the specific binding of the dye to the fibers, and τ_2=0.3ns corresponding to the dye in a viscous environment (see Supplementary figure 3C). Inset: Lineweaver-Burk graph of the bound DCVJ in relation to the concentration added to the sample.

J. Representative images of the ability of human CAFs (hCAFs) to contract collagen and quantification of contraction index. Contraction was performed during 3 days, and values are represented for the 3rd day.

K. Representative images of fibronectin fiber content in CDMs formed by hCAFs and quantification of the CDM thickness.

L. Analysis of fibronectin fiber orientation in CDMs formed by hCAFs.

Statistical significance was obtained using t-test: *$p < 0.05$; **$p < 0.01$; ***$p < 0.001$; ****$p < 0.0001$; n.s. non-significant.

Figure 4. CDMs Generated by RBD CAFs Exhibit Defects in Glycoprotein Composition.

(A) Volcano plot displaying differentially expressed peptides identified in the matrisome analysis of RAS-PI3K-deficient CDMs versus controls. The x-axis represents the log2 fold change (FC), and the y-axis shows the −log10 p-value. Downregulated peptides ($FC \geq 2$, $p < 0.05$) are in blue, upregulated peptides are in red, and non-significant peptides are in grey.

(B) Dendrogram showing expression values and sample distribution of the 35 differentially identified ECM components. The left side of the dendrogram depicts the division and category of the identified components.

(C) Chart showing the quantification of the different categories of matrisome components identified in RBD versus WT-derived CDMs.

(D) Functional enrichment analysis of significantly upregulated and downregulated peptides identified in the matrisome analysis of RBD *versus* WT CDMs.

(E) Representative images of Alcian Blue immunostaining of WT, RBD, RBD+p110α, and WT+Alpelisib-derived CDMs, indicating glycosylation levels.

(F) Relative gene expression levels of the indicated genes corresponding to altered glycoproteins in RBD versus WT fibroblasts (red bars) or WT treated with Verteporfin (green bars) in CAFs activated with TGF-β or conditioned medium (CM) from KPB6 cells. Error bars indicate mean ± SEM. Statistical significance was obtained using t-test: *$p < 0.05$; **$p < 0.01$; ***$p < 0.001$; ****$p < 0.0001$.

(G) Relative gene expression levels of the indicated genes corresponding to glycosylases identified in the RNA-seq analysis in RBD versus WT fibroblasts (red bars) or WT treated with Verteporfin (green bars) in CAFs activated with TGF-β or CM from KPB6 cells. Error bars indicate mean ± SEM. Statistical significance was obtained using t-test: *$p < 0.05$; **$p < 0.01$; ***$p < 0.001$; ****$p < 0.0001$.

Figure 5. Altered CDMs from PI3KRBD CAFs Modulate Tumor Cell Behavior.

(A) Representative images of KPB6 cells seeded onto decellularized CDMs formed by WT or RBD CAFs.

(B) Quantitative correlation analysis of KPB6 phalloidin (red) and fibronectin (grey) orientation in WT- or RBD-derived CDMs.

(C) Representative images of KPB6 focal adhesions identified by vinculin IF staining in the fibronectin fibers of WT- and RBD-derived CDMs. Graphs show the quantification of vinculin and fibronectin colocalization.

(D) Quantification of the directionality of KPB6 focal adhesions in WT- or RBD-derived CDMs.

(E) Relative gene expression levels of the indicated genes corresponding to EMT transcriptional programs in KPB6 cells reseeded in RBD-derived CDMs versus WT-derived CDMs. Error bars indicate mean ± SEM.

(F) Representative images and quantification graphs showing E-Cadherin protein expression in KPB6 cells seeded in WT- or RBD-derived CDMs. Three independent experiments were performed, and 80–100 cells per replicate were analyzed. Statistical significance was obtained using t-test: $^{**}p < 0.01$.

(G) Quantification of KPB6 proliferation rates when reseeded in decellularized WT (black line), RBD (red line), RBD+p110α (blue line), or WT+Alpelisib (green line)-derived CDMs.

(H) Representative images of human lung cancer cell line A549 seeded onto decellularized CDMs formed by hCAFs or hCAFs treated with Alpelisib.

(I) Quantification of A549 proliferation rates when reseeded in decellularized CDMs derived from hCAFs (black line) or hCAFs+Alpelisib (red line).

Statistical significance was obtained using t-test: $^{*}p < 0.05$; $^{**}p < 0.01$; $^{***}p < 0.001$; $^{****}p < 0.0001$.

Figure 6. Fibroblast-Specific RAS-PI3K Disruption Limits Tumor Growth and ECM Deposition in KRAS-Driven Lung Cancer.

(A) Representative H&E-stained lung sections from the *Pik3ca*^{fRBD} mouse model, showing specific fibroblast disruption of RAS-PI3K interaction, and quantification of tumor burden (tumor area as a percentage of total lung area) after tamoxifen treatment and KPB6 cell tail vein injection. Each dot represents an individual mouse. Lungs were analyzed 21 days after KPB6 injection.

(B) Kaplan-Meier survival curve depicting survival of *Pik3ca*$^{fRBD/-}$ mice following tamoxifen treatment and KPB6 cell tail vein injection.

(C) Representative lung sections with IHC staining for the indicated proteins (p-Histone H3, α-SMA, collagen, fibronectin and alcian blue) in mice after tamoxifen treatment and KPB6 injection.

(D) Graphs showing quantification of IHC-stained proteins analyzed in the previous panel.

(E) Representative H&E-stained lung sections from *Pik3ca*$^{fRBD/-}$ mice treated with either a combination of Cisplatin and Pemetrexed or the RAS inhibitor, RMC-7977. Quantification of tumor burden (tumor area as a percentage of total lung area) after two weeks of treatment is shown. Each dot represents an individual mouse.

REFERENCES

1. Sahai, E. *et al.* A framework for advancing our understanding of cancer-associated fibroblasts. *Nat Rev Cancer* **20**, 174-186 (2020).
2. Kalluri, R. The biology and function of fibroblasts in cancer. *Nat Rev Cancer* **16**, 582-598 (2016).
3. Baghban, R. *et al.* Tumor microenvironment complexity and therapeutic implications at a glance. *Cell Commun Signal* **18**, 59 (2020).
4. Caligiuri, G. & Tuveson, D.A. Activated fibroblasts in cancer: Perspectives and challenges. *Cancer Cell* **41**, 434-449 (2023).
5. Chen, X. & Song, E. Turning foes to friends: targeting cancer-associated fibroblasts. *Nat Rev Drug Discov* **18**, 99-115 (2019).
6. Cords, L. *et al.* Cancer-associated fibroblast classification in single-cell and spatial proteomics data. *Nat Commun* **14**, 4294 (2023).
7. Ma, C. *et al.* Pan-cancer spatially resolved single-cell analysis reveals the crosstalk between cancer-associated fibroblasts and tumor microenvironment. *Mol Cancer* **22**, 170 (2023).
8. Pally, D. & Naba, A. Extracellular matrix dynamics: A key regulator of cell migration across length-scales and systems. *Curr Opin Cell Biol* **86**, 102309 (2024).
9. Winkler, J., Abisoye-Ogunniyan, A., Metcalf, K.J. & Werb, Z. Concepts of extracellular matrix remodelling in tumour progression and metastasis. *Nat Commun* **11**, 5120 (2020).
10. Lu, P., Takai, K., Weaver, V.M. & Werb, Z. Extracellular matrix degradation and remodeling in development and disease. *Cold Spring Harb Perspect Biol* **3** (2011).
11. Orimo, A. *et al.* Stromal fibroblasts present in invasive human breast carcinomas promote tumor growth and angiogenesis through elevated SDF-1/CXCL12 secretion. *Cell* **121**, 335-348 (2005).
12. Liu, T. *et al.* Cancer-associated fibroblasts: an emerging target of anti-cancer immunotherapy. *J Hematol Oncol* **12**, 86 (2019).

13. Mao, X. *et al.* Crosstalk between cancer-associated fibroblasts and immune cells in the tumor microenvironment: new findings and future perspectives. *Mol Cancer* **20**, 131 (2021).

14. Valkenburg, K.C., de Groot, A.E. & Pienta, K.J. Targeting the tumour stroma to improve cancer therapy. *Nat Rev Clin Oncol* **15**, 366-381 (2018).

15. Tsoumakidou, M. The advent of immune stimulating CAFs in cancer. *Nat Rev Cancer* **23**, 258-269 (2023).

16. Kapeni, C. *et al.* Hedgehog signaling controls cytotoxic T cell migration in the tumour microenvironment. *Biorxiv* (2024).

17. Rhim, A.D. *et al.* Stromal elements act to restrain, rather than support, pancreatic ductal adenocarcinoma. *Cancer Cell* **25**, 735-747 (2014).

18. Lee, J.J. *et al.* Stromal response to Hedgehog signaling restrains pancreatic cancer progression. *Proc Natl Acad Sci U S A* **111**, E3091-3100 (2014).

19. Chen, Y., McAndrews, K.M. & Kalluri, R. Clinical and therapeutic relevance of cancer-associated fibroblasts. *Nat Rev Clin Oncol* **18**, 792-804 (2021).

20. Dias Carvalho, P. *et al.* KRAS Oncogenic Signaling Extends beyond Cancer Cells to Orchestrate the Microenvironment. *Cancer Res* **78**, 7-14 (2018).

21. Liu, Y., Xie, B. & Chen, Q. RAS signaling and immune cells: a sinister crosstalk in the tumor microenvironment. *J Transl Med* **21**, 595 (2023).

22. Boumelha, J. *et al.* CRISPR-Cas9 Screening Identifies KRAS-Induced COX2 as a Driver of Immunotherapy Resistance in Lung Cancer. *Cancer Res* **84**, 2231-2246 (2024).

23. Molina-Arcas, M. & Downward, J. Exploiting the therapeutic implications of KRAS inhibition on tumor immunity. *Cancer Cell* **42**, 338-357 (2024).

24. Hamarsheh, S., Gross, O., Brummer, T. & Zeiser, R. Immune modulatory effects of oncogenic KRAS in cancer. *Nat Commun* **11**, 5439 (2020).

25. Arbour, K.C. *et al.* Treatment Outcomes and Clinical Characteristics of Patients with KRAS-G12C-Mutant Non-Small Cell Lung Cancer. *Clin Cancer Res* **27**, 2209-2215 (2021).

26. Mills, L.D. *et al.* Loss of the transcription factor GLI1 identifies a signaling network in the tumor microenvironment mediating KRAS oncogene-induced transformation. *J Biol Chem* **288**, 11786-11794 (2013).

27. Ji, Z., Mei, F.C., Xie, J. & Cheng, X. Oncogenic KRAS activates hedgehog signaling pathway in pancreatic cancer cells. *J Biol Chem* **282**, 14048-14055 (2007).

28. Tape, C.J. *et al.* Oncogenic KRAS Regulates Tumor Cell Signaling via Stromal Reciprocation. *Cell* **165**, 1818 (2016).

29. Okada, F. *et al.* Impact of oncogenes in tumor angiogenesis: mutant K-ras up-regulation of vascular endothelial growth factor/vascular permeability factor is necessary, but not sufficient for tumorigenicity of human colorectal carcinoma cells. *Proc Natl Acad Sci U S A* **95**, 3609-3614 (1998).

30. Rak, J. *et al.* Mutant ras oncogenes upregulate VEGF/VPF expression: implications for induction and inhibition of tumor angiogenesis. *Cancer Res* **55**, 4575-4580 (1995).

31. Zhang, X., Gaspard, J.P. & Chung, D.C. Regulation of vascular endothelial growth factor by the Wnt and K-ras pathways in colonic neoplasia. *Cancer Res* **61**, 6050-6054 (2001).

32. Mehner, C. *et al.* Tumor cell-derived MMP3 orchestrates Rac1b and tissue alterations that promote pancreatic adenocarcinoma. *Mol Cancer Res* **12**, 1430-1439 (2014).

33. Robert, L. Tumors perturbing extracellular matrix biosynthesis. The case of von Recklinghausen's disease. *Pathol Biol (Paris)* **62**, 118-122 (2014).

34. Fujimura, K. *et al.* Eukaryotic Translation Initiation Factor 5A (EIF5A) Regulates Pancreatic Cancer Metastasis by Modulating RhoA and Rho-associated Kinase (ROCK) Protein Expression Levels. *J Biol Chem* **290**, 29907-29919 (2015).

35. Castellano, E. *et al.* Requirement for interaction of PI3-kinase p110alpha with RAS in lung tumor maintenance. *Cancer Cell* **24**, 617-630 (2013).

36. Murillo, M.M. *et al.* RAS interaction with PI3K p110alpha is required for tumor-induced angiogenesis. *J Clin Invest* **124**, 3601-3611 (2014).

37. Gupta, S. *et al.* Binding of ras to phosphoinositide 3-kinase p110alpha is required for ras-driven tumorigenesis in mice. *Cell* **129**, 957-968 (2007).

38. Castellano, E. *et al.* RAS signalling through PI3-Kinase controls cell migration via modulation of Reelin expression. *Nat Commun* **7**, 11245 (2016).

39. Johnson, L. *et al.* Somatic activation of the K-ras oncogene causes early onset lung cancer in mice. *Nature* **410**, 1111-1116 (2001).

40. Chandra Jena, B., Sarkar, S., Rout, L. & Mandal, M. The transformation of cancer-associated fibroblasts: Current perspectives on the role of TGF-beta in CAF mediated tumor progression and therapeutic resistance. *Cancer Lett* **520**, 222-232 (2021).

41. Calvo, F. *et al.* Cdc42EP3/BORG2 and Septin Network Enables Mechano-transduction and the Emergence of Cancer-Associated Fibroblasts. *Cell Rep* **13**, 2699-2714 (2015).

42. Naktubtim, C., Payuhakrit, W., Uttarawichien, T., Hassametto, A. & Suwannalert, P. YAP, a novel target regulates F-actin rearrangement-associated CAFs transformation and promotes colorectal cancer cell progression. *Biomed Pharmacother* **155**, 113757 (2022).

43. Nurmik, M., Ullmann, P., Rodriguez, F., Haan, S. & Letellier, E. In search of definitions: Cancer-associated fibroblasts and their markers. *Int J Cancer* **146**, 895-905 (2020).

44. Calvo, F. *et al.* Mechanotransduction and YAP-dependent matrix remodelling is required for the generation and maintenance of cancer-associated fibroblasts. *Nat Cell Biol* **15**, 637-646 (2013).

45. Qiao, Y. *et al.* YAP Regulates Actin Dynamics through ARHGAP29 and Promotes Metastasis. *Cell Rep* **19**, 1495-1502 (2017).

46. Song, H. *et al.* YAP1 Inhibition Induces Phenotype Switching of Cancer-Associated Fibroblasts to Tumor Suppressive in Prostate Cancer. *Cancer Res* **84**, 3728-3742 (2024).

47. Franco-Barraza, J., Beacham, D.A., Amatangelo, M.D. & Cukierman, E. Preparation of Extracellular Matrices Produced by Cultured and Primary Fibroblasts. *Curr Protoc Cell Biol* **71**, 10 19 11-10 19 34 (2016).

48. Biancalana, M. & Koide, S. Molecular mechanism of Thioflavin-T binding to amyloid fibrils. *Biochim Biophys Acta* **1804**, 1405-1412 (2010).

49. Nagarajan, S. & Lapidus, L.J. Fluorescent Probe DCVJ Shows High Sensitivity for Characterization of Amyloid beta-Peptide Early in the Lag Phase. *Chembiochem* **18**, 2205-2211 (2017).

50. Iio, T., Itakura, M., Takahashi, S. & Sawada, S. 9-(Dicyanovinyl)julolidine binding to bovine brain calmodulin. *J Biochem* **109**, 499-502 (1991).

51. De Luca, G. *et al.* Probing ensemble polymorphism and single aggregate structural heterogeneity in insulin amyloid self-assembly. *J Colloid Interface Sci* **574**, 229-240 (2020).

52. Naba, A. *et al.* The extracellular matrix: Tools and insights for the "omics" era. *Matrix Biol* **49**, 10-24 (2016).

53. Shao, X. *et al.* MatrisomeDB 2.0: 2023 updates to the ECM-protein knowledge database. *Nucleic Acids Res* **51**, D1519-D1530 (2023).

54. Gyorffy, B. Transcriptome-level discovery of survival-associated biomarkers and therapy targets in non-small-cell lung cancer. *Br J Pharmacol* **181**, 362-374 (2024).

55. Brabletz, S., Schuhwerk, H., Brabletz, T. & Stemmler, M.P. Dynamic EMT: a multi-tool for tumor progression. *EMBO J* **40**, e108647 (2021).

56. Moreno-Bueno, G., Portillo, F. & Cano, A. Transcriptional regulation of cell polarity in EMT and cancer. *Oncogene* **27**, 6958-6969 (2008).

57. Yuan, Z. *et al.* Extracellular matrix remodeling in tumor progression and immune escape: from mechanisms to treatments. *Mol Cancer* **22**, 48 (2023).

58. Jiang, Y. *et al.* Targeting extracellular matrix stiffness and mechanotransducers to improve cancer therapy. *J Hematol Oncol* **15**, 34 (2022).

59. Soriano, O., Alcon-Perez, M., Vicente-Manzanares, M. & Castellano, E. The Crossroads between RAS and RHO Signaling Pathways in Cellular Transformation, Motility and Contraction. *Genes (Basel)* **12** (2021).

60. Deng, S. *et al.* PI3K/AKT Signaling Tips the Balance of Cytoskeletal Forces for Cancer Progression. *Cancers (Basel)* **14** (2022).

61. Angulo-Urarte, A. *et al.* Endothelial cell rearrangements during vascular patterning require PI3-kinase-mediated inhibition of actomyosin contractility. *Nat Commun* **9**, 4826 (2018).

62. Crackower, M.A. *et al.* Regulation of myocardial contractility and cell size by distinct PI3K-PTEN signaling pathways. *Cell* **110**, 737-749 (2002).

63. Schwarz, U.S. & Gardel, M.L. United we stand: integrating the actin cytoskeleton and cell-matrix adhesions in cellular mechanotransduction. *J Cell Sci* **125**, 3051-3060 (2012).

64. Martino, F., Perestrelo, A.R., Vinarsky, V., Pagliari, S. & Forte, G. Cellular Mechanotransduction: From Tension to Function. *Front Physiol* **9**, 824 (2018).

65. Dupont, S. Role of YAP/TAZ in cell-matrix adhesion-mediated signalling and mechanotransduction. *Exp Cell Res* **343**, 42-53 (2016).

66. Mason, D.E. *et al.* YAP and TAZ limit cytoskeletal and focal adhesion maturation to enable persistent cell motility. *J Cell Biol* **218**, 1369-1389 (2019).

67. Chen, C. *et al.* Single-cell and spatial transcriptomics reveal POSTN(+) cancer-associated fibroblasts correlated with immune suppression and tumour progression in non-small cell lung cancer. *Clin Transl Med* **13**, e1515 (2023).

68. Foster, D.S. *et al.* Multiomic analysis reveals conservation of cancer-associated fibroblast phenotypes across species and tissue of origin. *Cancer Cell* **40**, 1392-1406 e1397 (2022).

69. Low, B.C. *et al.* YAP/TAZ as mechanosensors and mechanotransducers in regulating organ size and tumor growth. *FEBS Lett* **588**, 2663-2670 (2014).

70. Cox, T.R. The matrix in cancer. *Nat Rev Cancer* **21**, 217-238 (2021).

71. Bonnans, C., Chou, J. & Werb, Z. Remodelling the extracellular matrix in development and disease. *Nat Rev Mol Cell Biol* **15**, 786-801 (2014).

72. Brassart-Pasco, S. *et al.* Tumor Microenvironment: Extracellular Matrix Alterations Influence Tumor Progression. *Front Oncol* **10**, 397 (2020).

73. Nabeya, Y. *et al.* Serum cross-linked carboxyterminal telopeptide of type I collagen (ICTP) as a prognostic tumor marker in patients with esophageal squamous cell carcinoma. *Cancer* **94**, 940-949 (2002).

74. Jaaskelainen, A., Jukkola, A., Risteli, J., Haapasaari, K.M. & Karihtala, P. Elevated preoperative serum levels of collagen I carboxyterminal telopeptide predict better outcome in early-stage luminal-B-like (HER2-negative) and triple-negative subtypes of breast cancer. *Tumour Biol* **41**, 1010428319847081 (2019).

75. Plebani, M. *et al.* N-terminal peptide of type III procollagen: a possible predictor of colorectal carcinoma recurrence. *Cancer* **79**, 1299-1303 (1997).

76. Willumsen, N. *et al.* Extracellular matrix specific protein fingerprints measured in serum can separate pancreatic cancer patients from healthy controls. *BMC Cancer* **13**, 554 (2013).

77. Liu, N. *et al.* Metastatin: a hyaluronan-binding complex from cartilage that inhibits tumor growth. *Cancer Res* **61**, 1022-1028 (2001).

78. Brezillon, S., Pietraszek, K., Maquart, F.X. & Wegrowski, Y. Lumican effects in the control of tumour progression and their links with metalloproteinases and integrins. *FEBS J* **280**, 2369-2381 (2013).

79. Karamanos, N.K. *et al.* Proteoglycan Chemical Diversity Drives Multifunctional Cell Regulation and Therapeutics. *Chem Rev* **118**, 9152-9232 (2018).

80. Barbazan, J. *et al.* Cancer-associated fibroblasts actively compress cancer cells and modulate mechanotransduction. *Nat Commun* **14**, 6966 (2023).

81. Eble, J.A. & Niland, S. The extracellular matrix in tumor progression and metastasis. *Clin Exp Metastasis* **36**, 171-198 (2019).

82. Elgundi, Z. *et al.* Cancer Metastasis: The Role of the Extracellular Matrix and the Heparan Sulfate Proteoglycan Perlecan. *Front Oncol* **9**, 1482 (2019).

83. Kaushik, S., Pickup, M.W. & Weaver, V.M. From transformation to metastasis: deconstructing the extracellular matrix in breast cancer. *Cancer Metastasis Rev* **35**, 655-667 (2016).

84. Prakash, J. & Shaked, Y. The Interplay between Extracellular Matrix Remodeling and Cancer Therapeutics. *Cancer Discov* **14**, 1375-1388 (2024).

85. Erdogan, B. *et al.* Cancer-associated fibroblasts promote directional cancer cell migration by aligning fibronectin. *J Cell Biol* **216**, 3799-3816 (2017).

86. Karamanos, N.K. *et al.* A guide to the composition and functions of the extracellular matrix. *FEBS J* **288**, 6850-6912 (2021).

87. Stylianopoulos, T., Munn, L.L. & Jain, R.K. Reengineering the Physical Microenvironment of Tumors to Improve Drug Delivery and Efficacy: From Mathematical Modeling to Bench to Bedside. *Trends Cancer* **4**, 292-319 (2018).

88. Datta, M., Coussens, L.M., Nishikawa, H., Hodi, F.S. & Jain, R.K. Reprogramming the Tumor Microenvironment to Improve Immunotherapy: Emerging Strategies and Combination Therapies. *Am Soc Clin Oncol Educ Book* **39**, 165-174 (2019).

89. Mongiat, M., Andreuzzi, E., Tarticchio, G. & Paulitti, A. Extracellular Matrix, a Hard Player in Angiogenesis. *Int J Mol Sci* **17** (2016).

90. Dejana, E. *et al.* Interaction between fibrinogen and cultured endothelial cells. Induction of migration and specific binding. *J Clin Invest* **75**, 11-18 (1985).

91. Senger, D.R. *et al.* The alpha(1)beta(1) and alpha(2)beta(1) integrins provide critical support for vascular endothelial growth factor signaling, endothelial cell migration, and tumor angiogenesis. *Am J Pathol* **160**, 195-204 (2002).

92. Lawler, P.R. & Lawler, J. Molecular basis for the regulation of angiogenesis by thrombospondin-1 and -2. *Cold Spring Harb Perspect Med* **2**, a006627 (2012).

93. Sapudom, J., Alatoom, A., Tipay, P.S. & Teo, J.C. Matrix stiffening from collagen fibril density and alignment modulates YAP-mediated T-cell immune suppression. *Biomaterials* **315**, 122900 (2025).

94. Sutherland, T.E., Dyer, D.P. & Allen, J.E. The extracellular matrix and the immune system: A mutually dependent relationship. *Science* **379**, eabp8964 (2023).

95. Chhabra, Y. & Weeraratna, A.T. Fibroblasts in cancer: Unity in heterogeneity. *Cell* **186**, 1580-1609 (2023).

96. Cannon, A. *et al.* Desmoplasia in pancreatic ductal adenocarcinoma: insight into pathological function and therapeutic potential. *Genes Cancer* **9**, 78-86 (2018).

97. Tian, C. *et al.* Suppression of pancreatic ductal adenocarcinoma growth and metastasis by fibrillar collagens produced selectively by tumor cells. *Nat Commun* **12**, 2328 (2021).

98. Cazet, A.S. *et al.* Targeting stromal remodeling and cancer stem cell plasticity overcomes chemoresistance in triple negative breast cancer. *Nat Commun* **9**, 2897 (2018).

99. Downward, J. Targeting RAS signalling pathways in cancer therapy. *Nat Rev Cancer* **3**, 11-22 (2003).

100. Fernandez-Medarde, A. & Santos, E. Ras in cancer and developmental diseases. *Genes Cancer* **2**, 344-358 (2011).

101. Holderfield, M. *et al.* Concurrent inhibition of oncogenic and wild-type RAS-GTP for cancer therapy. *Nature* **629**, 919-926 (2024).

102. Serrano, M., Lin, A.W., McCurrach, M.E., Beach, D. & Lowe, S.W. Oncogenic ras provokes premature cell senescence associated with accumulation of p53 and p16INK4a. *Cell* **88**, 593-602 (1997).

103. Bahar, M.E., Kim, H.J. & Kim, D.R. Targeting the RAS/RAF/MAPK pathway for cancer therapy: from mechanism to clinical studies. *Signal Transduct Target Ther* **8**, 455 (2023).

104. Casado, P. *et al.* Integrative phosphoproteomics defines two biologically distinct groups of KMT2A rearranged acute myeloid leukaemia with different drug response phenotypes. *Signal Transduct Target Ther* **8**, 80 (2023).

105. Casado, P. *et al.* Kinase-substrate enrichment analysis provides insights into the heterogeneity of signaling pathway activation in leukemia cells. *Sci Signal* **6**, rs6 (2013).

106. Hijazi, M., Smith, R., Rajeeve, V., Bessant, C. & Cutillas, P.R. Reconstructing kinase network topologies from phosphoproteomics data reveals cancer-associated rewiring. *Nat Biotechnol* **38**, 493-502 (2020).

107. Alcolea, M.P., Casado, P., Rodriguez-Prados, J.C., Vanhaesebroeck, B. & Cutillas, P.R. Phosphoproteomic analysis of leukemia cells under basal and drug-treated conditions identifies markers of kinase pathway activation and mechanisms of resistance. *Mol Cell Proteomics* **11**, 453-466 (2012).

108. Cutillas, P.R. & Vanhaesebroeck, B. Quantitative profile of five murine core proteomes using label-free functional proteomics. *Mol Cell Proteomics* **6**, 1560-1573 (2007).

109. Montoya, A., Beltran, L., Casado, P., Rodriguez-Prados, J.C. & Cutillas, P.R. Characterization of a TiO(2) enrichment method for label-free quantitative phosphoproteomics. *Methods* **54**, 370-378 (2011).

110. Larsen, M.R., Thingholm, T.E., Jensen, O.N., Roepstorff, P. & Jorgensen, T.J. Highly selective enrichment of phosphorylated peptides from peptide mixtures using titanium dioxide microcolumns. *Mol Cell Proteomics* **4**, 873-886 (2005).

111. Gene Ontology, C. *et al.* The Gene Ontology knowledgebase in 2023. *Genetics* **224** (2023).

112. Kanehisa, M. & Goto, S. KEGG: kyoto encyclopedia of genes and genomes. *Nucleic Acids Res* **28**, 27-30 (2000).

113. Wu, T. *et al.* clusterProfiler 4.0: A universal enrichment tool for interpreting omics data. *Innovation (Camb)* **2**, 100141 (2021).

114. Johnson, J.L. *et al.* An atlas of substrate specificities for the human serine/threonine kinome. *Nature* **613**, 759-766 (2023).

115. Patro, R., Duggal, G., Love, M.I., Irizarry, R.A. & Kingsford, C. Salmon provides fast and bias-aware quantification of transcript expression. *Nat Methods* **14**, 417-419 (2017).

116. Robinson, M.D., McCarthy, D.J. & Smyth, G.K. edgeR: a Bioconductor package for differential expression analysis of digital gene expression data. *Bioinformatics* **26**, 139-140 (2010).

117. Yu, G., Wang, L.G., Han, Y. & He, Q.Y. clusterProfiler: an R package for comparing biological themes among gene clusters. *OMICS* **16**, 284-287 (2012).

118. Jorba, I., Uriarte, J.J., Campillo, N., Farre, R. & Navajas, D. Probing Micromechanical Properties of the Extracellular Matrix of Soft Tissues by Atomic Force Microscopy. *J Cell Physiol* **232**, 19-26 (2017).

119. Rico, F. *et al.* Probing mechanical properties of living cells by atomic force microscopy with blunted pyramidal cantilever tips. *Phys Rev E Stat Nonlin Soft Matter Phys* **72**, 021914 (2005).

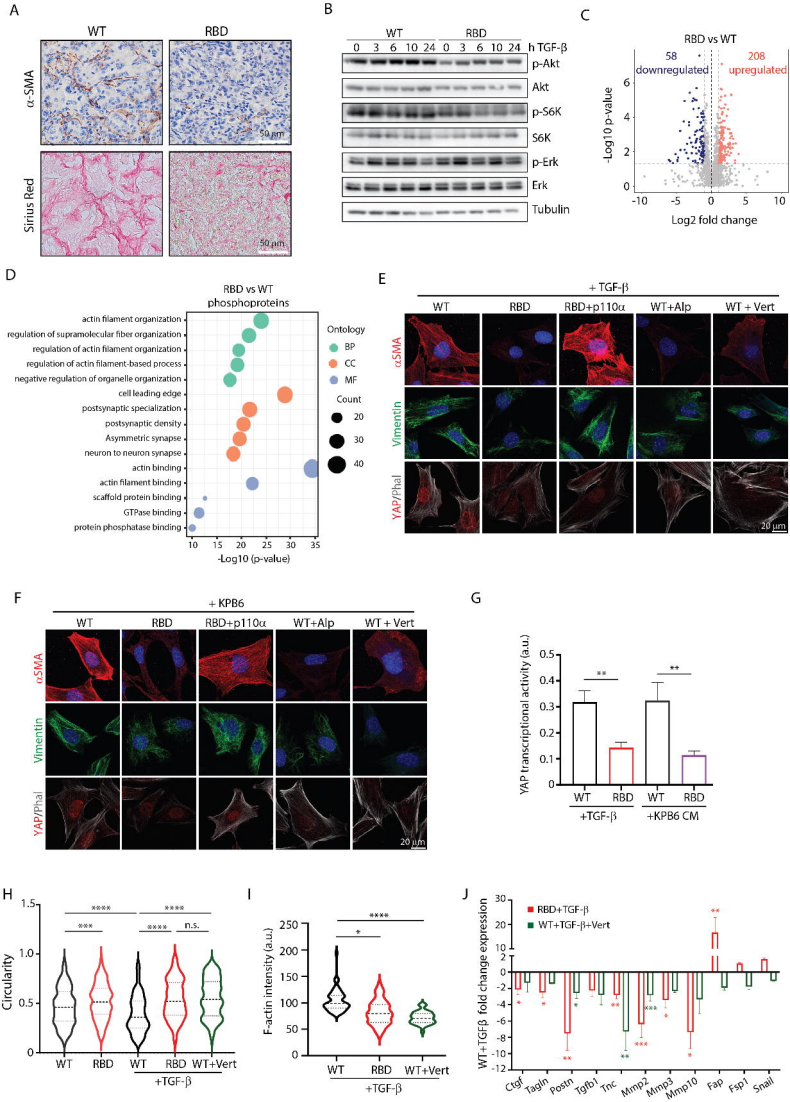
A
WT
RBD
α-SMA
Sirius Red
50 µm
B
WT
RBD
0 3 6 10 24 0 3 6 10 24 h TGF-β
p-Akt
Akt
p-S6K
S6K
p-Erk
Erk
Tubulin
C
RBD vs WT
58 downregulated
208 upregulated
-Log10 p-value
Log2 fold change
D
RBD vs WT phosphoproteins
actin filament organization
regulation of supramolecular fiber organization
regulation of actin filament organization
regulation of actin filament-based process
negative regulation of organelle organization
cell leading edge
postsynaptic specialization
postsynaptic density
Asymmetric synapse
neuron to neuron synapse
actin binding
actin filament binding
scaffold protein binding
GTPase binding
protein phosphatase binding
Ontology
BP
CC
MF
Count
20
30
40
-Log10 (p-value)
E
+ TGF-β
WT
RBD
RBD+p110α
WT+Alp
WT + Vert
αSMA
Vimentin
YAP/Phal
20 µm
F
+ KPB6
WT
RBD
RBD+p110α
WT+Alp
WT + Vert
αSMA
Vimentin
YAP/Phal
20 µm
G
YAP transcriptional activity (a.u.)
WT
RBD
WT
RBD
+TGF-β
+KPB6 CM
H
Circularity
WT
RBD
WT
RBD
WT+Vert
+TGF-β
n.s.
I
F-actin intensity (a.u.)
WT
RBD
WT+Vert
+TGF-β
J
RBD+TGF-β
WT+TGF-β+Vert
WT+TGFβ fold change expression
Ctgf
Tagln
Postn
Tgfb1
Tnc
Mmp2
Mmp3
Mmp10
Fap
Fsp1
Snail

A

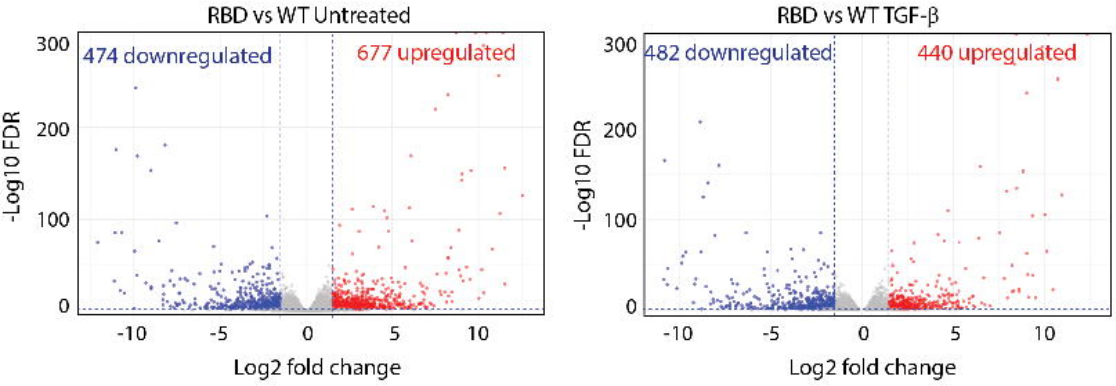
RBD vs WT Untreated
474 downregulated
677 upregulated
-Log10 FDR
Log2 fold change
RBD vs WT TGF-β
482 downregulated
440 upregulated
-Log10 FDR
Log2 fold change

B

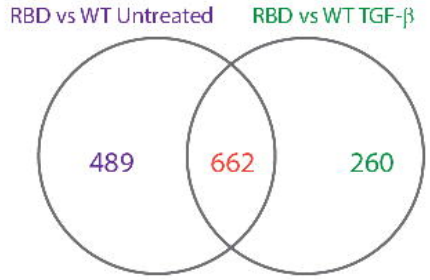
RBD vs WT Untreated
RBD vs WT TGF-β
489
662
260

C

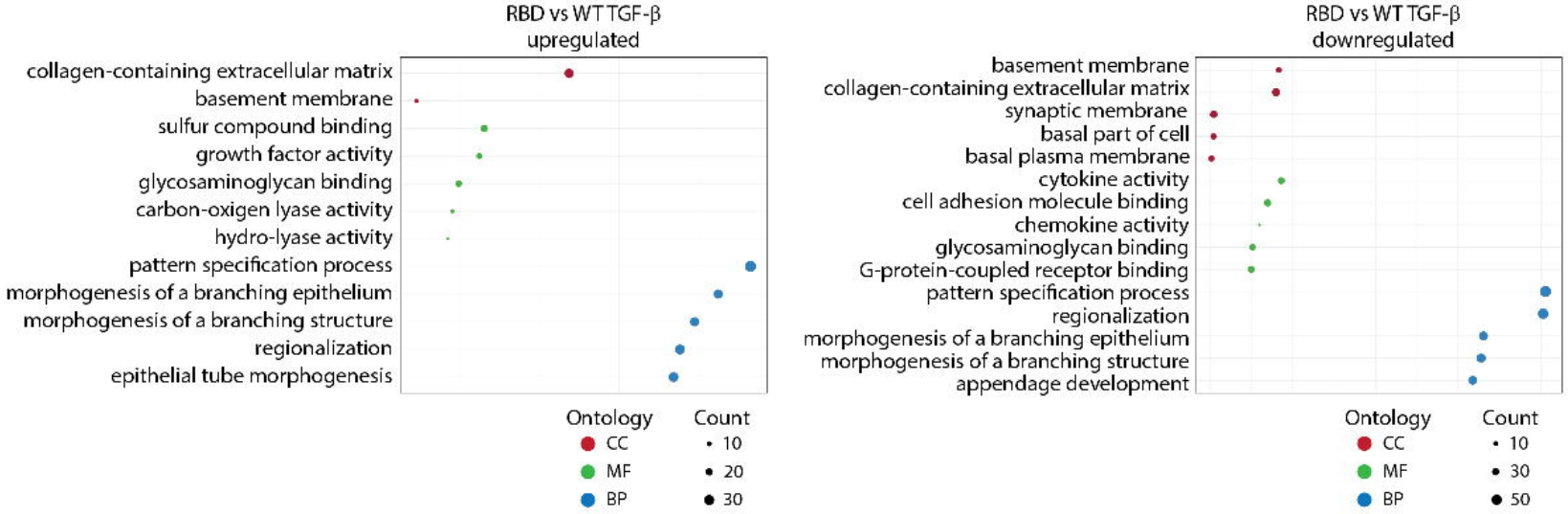
RBD vs WT TGF-β
upregulated
collagen-containing extracellular matrix
basement membrane
sulfur compound binding
growth factor activity
glycosaminoglycan binding
carbon-oxigen lyase activity
hydro-lyase activity
pattern specification process
morphogenesis of a branching epithelium
morphogenesis of a branching structure
regionalization
epithelial tube morphogenesis
Ontology
CC
MF
BP
Count
10
20
30
RBD vs WT TGF-β
downregulated
basement membrane
collagen-containing extracellular matrix
synaptic membrane
basal part of cell
basal plasma membrane
cytokine activity
cell adhesion molecule binding
chemokine activity
glycosaminoglycan binding
G-protein-coupled receptor binding
pattern specification process
regionalization
morphogenesis of a branching epithelium
morphogenesis of a branching structure
appendage development
Ontology
CC
MF
BP
Count
10
30
50

D

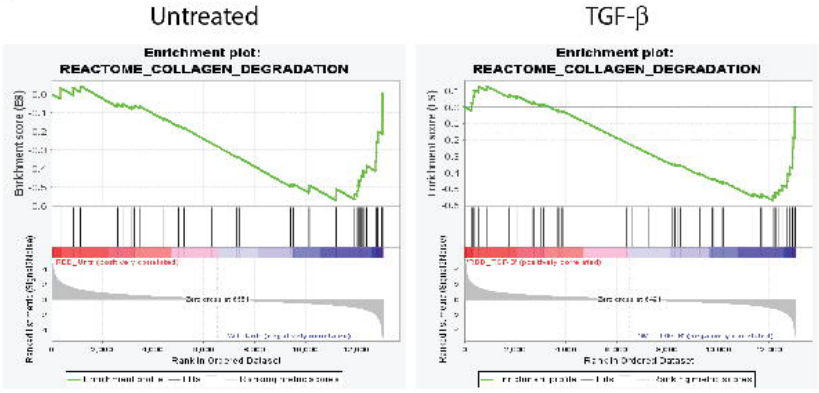
Untreated
Enrichment plot:
REACTOME_COLLAGEN_DEGRADATION
TGF-β
Enrichment plot:
REACTOME_COLLAGEN_DEGRADATION

E

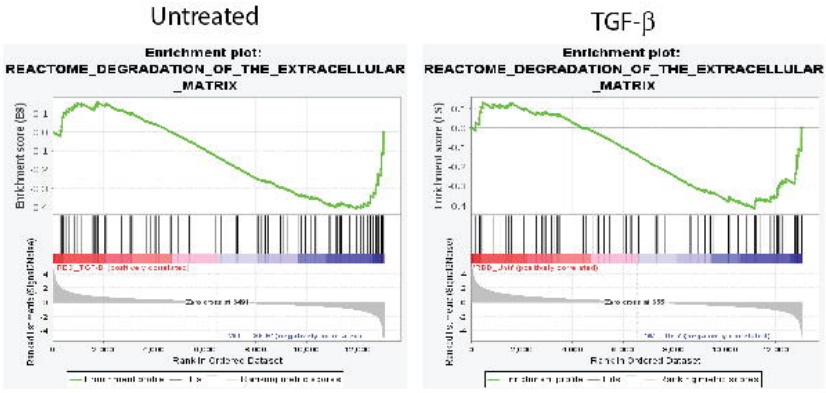
Untreated
Enrichment plot:
REACTOME_DEGRADATION_OF_THE_EXTRACELLULAR_MATRIX
TGF-β
Enrichment plot:
REACTOME_DEGRADATION_OF_THE_EXTRACELLULAR_MATRIX

F

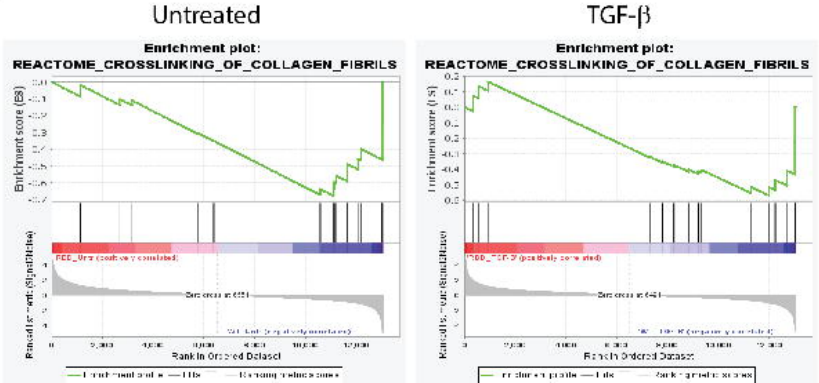
Untreated
Enrichment plot:
REACTOME_CROSSLINKING_OF_COLLAGEN_FIBRILS
TGF-β
Enrichment plot:
REACTOME_CROSSLINKING_OF_COLLAGEN_FIBRILS

G

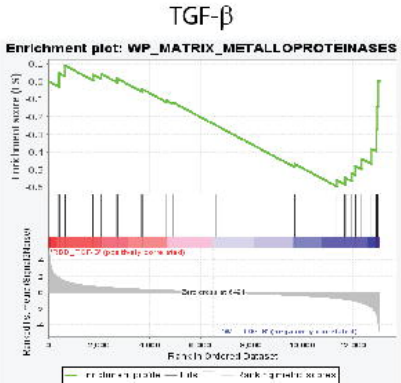
TGF-β
Enrichment plot: WP_MATRIX_METALLOPROTEINASES

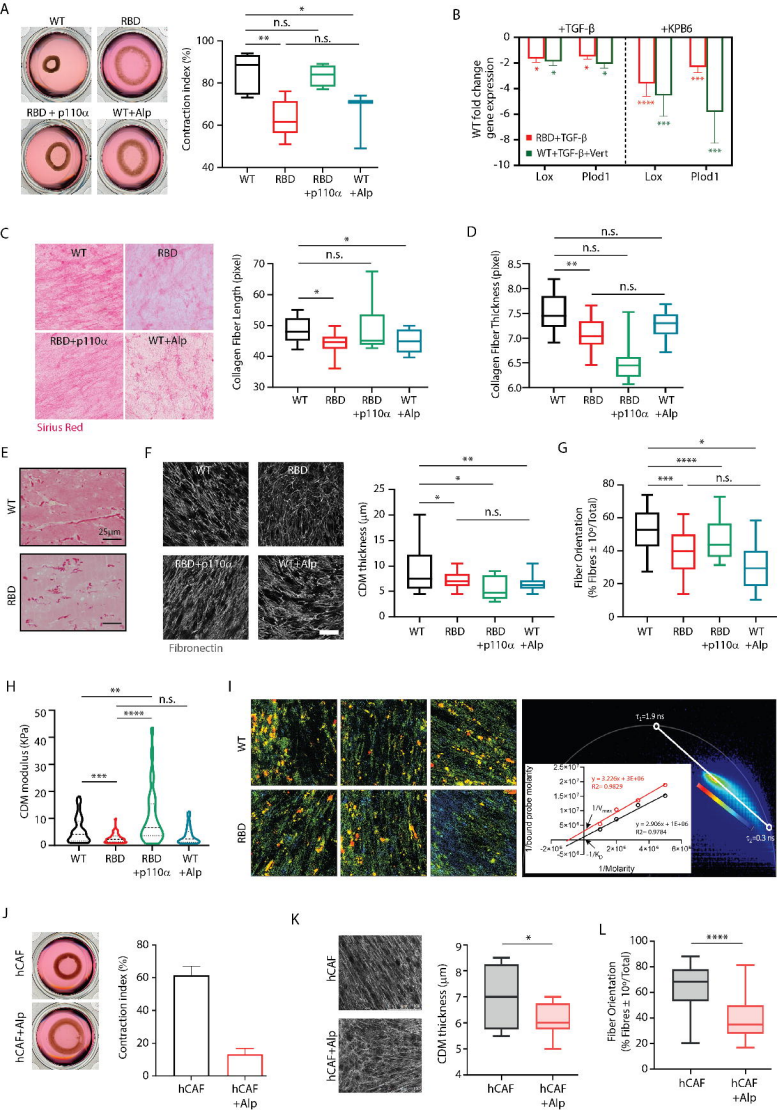
A
WT
RBD
RBD + p110α
WT+Alp
Contraction index (%)
n.s.
**
*
n.s.
WT
RBD
RBD +p110α
WT +Alp
B
+TGF-β
+KPB6
WT fold change gene expression
RBD+TGF-β
WT+TGF-β+Vert
Lox
Plod1
Lox
Plod1
C
WT
RBD
RBD+p110α
WT+Alp
Sirius Red
Collagen Fiber Length (pixel)
D
Collagen Fiber Thickness (pixel)
E
WT
RBD
25μm
F
WT
RBD
RBD+p110α
WT+Alp
Fibronectin
CDM thickness (μm)
G
Fiber Orientation (% Fibres ± 10°/Total)
H
CDM modulus (kPa)
I
WT
RBD
J
hCAF
hCAF+Alp
Contraction index (%)
K
CDM thickness (μm)
L
Fiber Orientation (% Fibres ± 10°/Total)

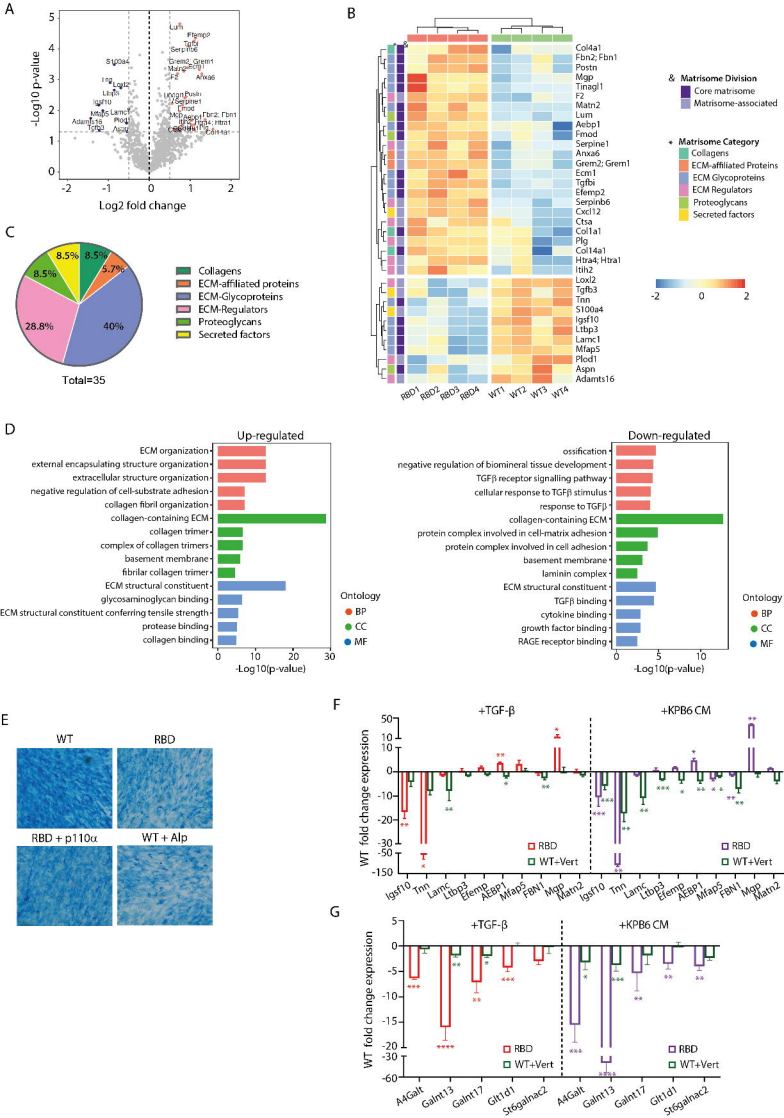
A
-Log10 p-value
Log2 fold change
Lum
Ifitm2
Tgfbi
Serpinb6
Grem2; Grem1
Mmp2
F2
Anxa6
S100a4
Ecm1
Ctsa
Lgals3
Lbp
Igfbp10
Serpine1
Lamc1
Mfap5
Lamc2
Fbn2
Fbn1
Adamts16
Tgfb3
Aspn
Postn
Col14a1
B
Col4a1
Fbn2; Fbn1
Postn
Mgp
Tinagl1
F2
Matn2
Lum
Aebp1
Fmod
Serpine1
Anxa6
Grem2; Grem1
Ecm1
Tgfbi
Efemp2
Serpinb6
Cxcl12
Ctsa
Col1a1
Plg
Col14a1
Htra4; Htra1
Itih2
Loxl2
Tgfb3
Tnn
S100a4
Igsf10
Ltbp3
Lamc1
Mfap5
Plod1
Aspn
Adamts16
RBD1
RBD2
RBD3
RBD4
WT1
WT2
WT3
WT4
& Matrisome Division
Core matrisome
Matrisome-associated
* Matrisome Category
Collagens
ECM-affiliated Proteins
ECM Glycoproteins
ECM Regulators
Proteoglycans
Secreted factors
-2
0
2
C
8.5%
5.7%
40%
28.8%
8.5%
8.5%
Collagens
ECM-affiliated proteins
ECM-Glycoproteins
ECM-Regulators
Proteoglycans
Secreted factors
Total=35
D
Up-regulated
ECM organization
external encapsulating structure organization
extracellular structure organization
negative regulation of cell-substrate adhesion
collagen fibril organization
collagen-containing ECM
collagen trimer
complex of collagen trimers
basement membrane
fibrillar collagen trimer
ECM structural constituent
glycosaminoglycan binding
ECM structural constituent conferring tensile strength
protease binding
collagen binding
-Log10(p-value)
Down-regulated
ossification
negative regulation of biomineral tissue development
TGFβ receptor signalling pathway
cellular response to TGFβ stimulus
response to TGFβ
collagen-containing ECM
protein complex involved in cell-matrix adhesion
protein complex involved in cell adhesion
basement membrane
laminin complex
ECM structural constituent
TGFβ binding
cytokine binding
growth factor binding
RAGE receptor binding
-Log10(p-value)
Ontology
BP
CC
MF
E
WT
RBD
RBD + p110α
WT + Alp
F
+TGF-β
+KPB6 CM
WT fold change expression
RBD
WT+Vert
Igsf10
Tnn
Lamc1
Ltbp3
Efemp2
Abp1
Mfap5
FBN1
Mgp
Matn2
G
+TGF-β
+KPB6 CM
WT fold change expression
RBD
WT+Vert
A4GalT
GalNT13
GalNT17
Glt1d1
St6galnac2

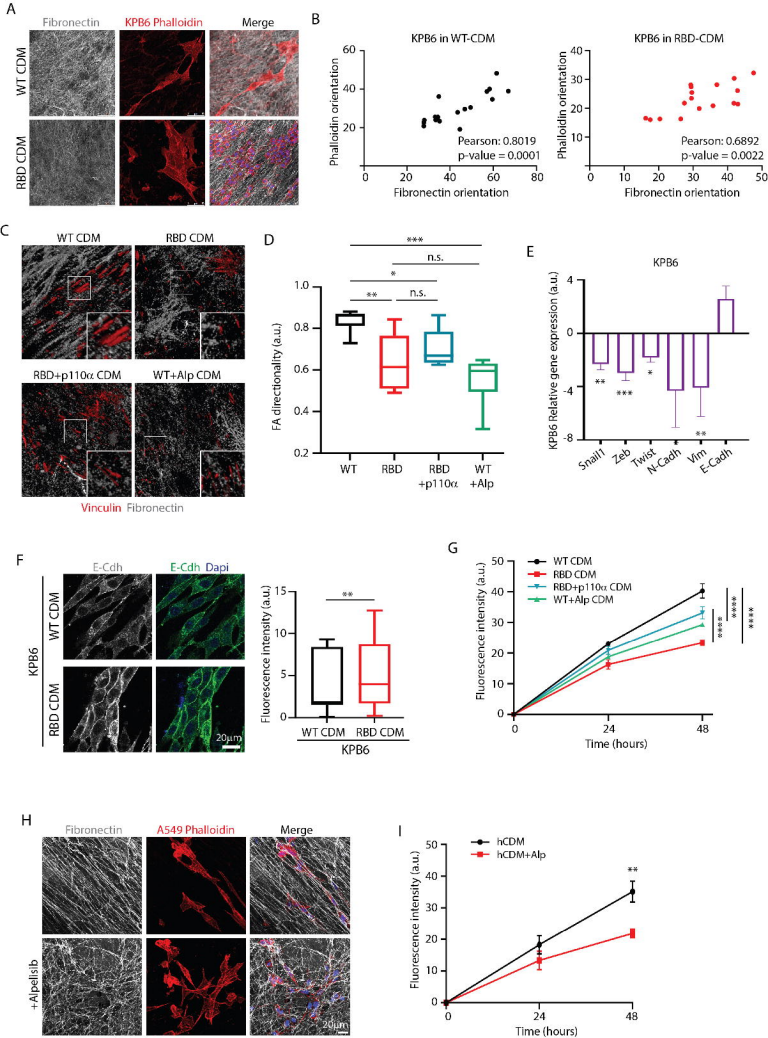
A
Fibronectin
KPB6 Phalloidin
Merge
WT CDM
RBD CDM
B
KPB6 in WT-CDM
Phalloidin orientation
Fibronectin orientation
Pearson: 0.8019
p-value = 0.0001
KPB6 in RBD-CDM
Pearson: 0.6892
p-value = 0.0022
C
WT CDM
RBD CDM
RBD+p110α CDM
WT+Alp CDM
Vinculin Fibronectin
D
FA directionality (a.u.)
WT
RBD
RBD +p110α
WT +Alp
n.s.
E
KPB6
KPB6 Relative gene expression (a.u.)
Snail1
Zeb
Twist
N-Cadh
Vim
E-Cadh
F
E-Cdh
E-Cdh Dapi
KPB6
WT CDM
RBD CDM
20μm
Fluorescence intensity (a.u.)
G
WT CDM
RBD CDM
RBD+p110α CDM
WT+Alp CDM
Fluorescence intensity (a.u.)
Time (hours)
H
Fibronectin
A549 Phalloidin
Merge
+Alpelisib
20μm
I
hCDM
hCDM+Alp
Fluorescence intensity (a.u.)
Time (hours)

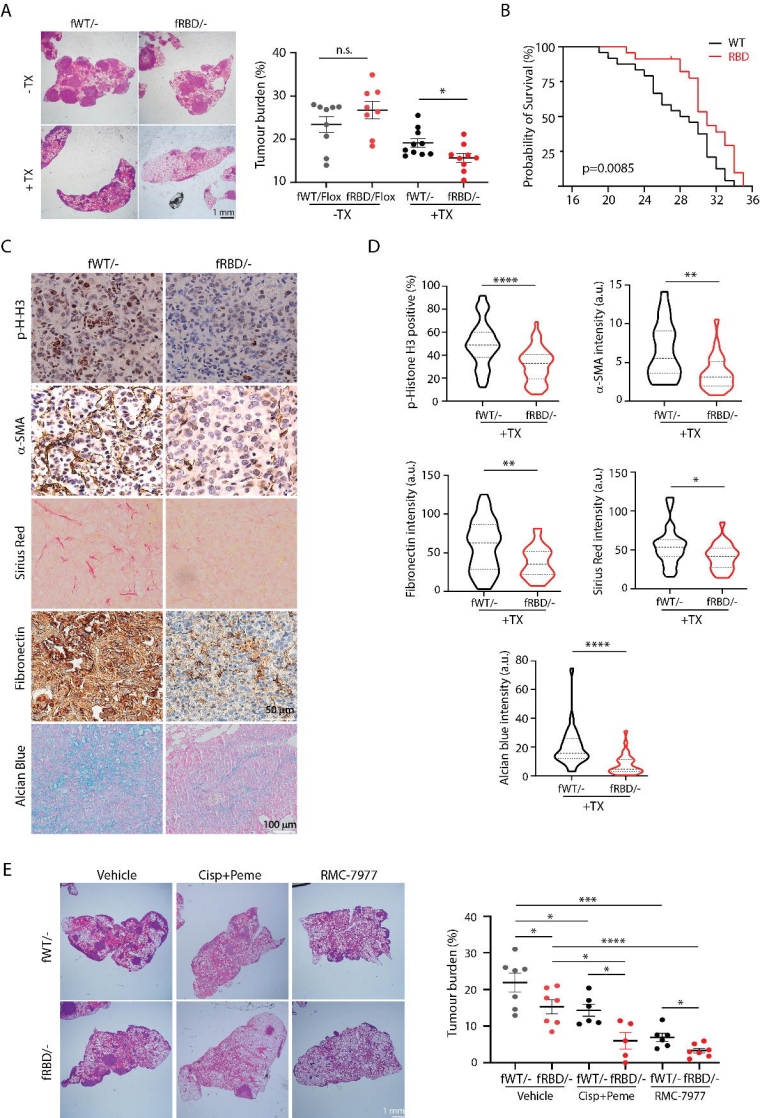
A
fWT/-
fRBD/-
-TX
+TX
1 mm
Tumour burden (%)
n.s.
*
fWT/Flox
fRBD/Flox
fWT/-
fRBD/-
-TX
+TX
B
Probability of Survival (%)
WT
RBD
p=0.0085
C
fWT/-
fRBD/-
p-H-H3
α-SMA
Sirius Red
Fibronectin
Alcian Blue
50 µm
100 µm
D
p-Histone H3 positive (%)
****
α-SMA intensity (a.u.)
**
Fibronectin intensity (a.u.)
**
Sirius Red intensity (a.u.)
*
Alcian blue intensity (a.u.)
****
fWT/-
fRBD/-
+TX
E
Vehicle
Cisp+Peme
RMC-7977
fWT/-
fRBD/-
1 mm
Tumour burden (%)
***
*
****
Vehicle
Cisp+Peme
RMC-7977